Monthly Notices
of the
ROYAL ASTRONOMICAL SOCIETY

MNRAS **481,** 4548–4565 (2018)
Advance Access publication 2018 September 27

doi:10.1093/mnras/sty2521

The Lockman Hole Project: new constraints on the sub-mJy source counts from a wide-area 1.4 GHz mosaic

I. Prandoni [1]★ G. Guglielmino,[1,2] R. Morganti [3,4] M. Vaccari [1,5] A. Maini,[1,2,6,7] H. J. A. Röttgering,[8] M. J. Jarvis[5,9] and M. A. Garrett[10,11]

[1]*INAF – Istituto di Radioastronomia, via Gobetti 101, I-40129 Bologna, Italy*
[2]*DIFA, University of Bologna, Via Ranzani 2, I-40126 Bologna, Italy*
[3]*ASTRON, the Netherlands Institute of Radio Astronomy, Postbus 2, NL-7990 AA, Dwingeloo, the Netherlands*
[4]*Kapteyn Astronomical Institute, University of Groningen, PO Box 800, NL-9700 AV Groningen, the Netherlands*
[5]*Department of Physics and Astronomy, University of the Western Cape, Bellville 7535, Cape Town, South Africa*
[6]*Department of Physics and Astronomy, Macquarie University, Balaclava Road, North Ryde, NSW 2109, Australia*
[7]*CSIRO Astronomy and Space Science, PO Box 76, Epping, NSW 1710, Australia*
[8]*Leiden Observatory, Leiden University, PO Box 9513, NL-2300 RA Leiden, the Netherlands*
[9]*Oxford Astrophysics, Denys Wilkinson Building, Keble Road, Oxford OX1 3RH, UK*
[10]*School of Physics and Astronomy, University of Manchester,The Alan Turing Building, Oxford Road, Oxford M13 9PL, UK*
[11]*Jodrell Bank Observatory, Lower Withington, University of Manchester, Macclesfield, Cheshire SK11 9DL, UK*

Accepted 2018 September 11. Received 2018 September 6; in original form 2018 May 31

ABSTRACT

This paper is part of a series discussing the results obtained in the framework of a wide international collaboration – the Lockman Hole Project – aimed at improving the extensive multiband coverage available in the Lockman Hole region, through novel deep, wide-area, multifrequency (60, 150, 350 MHz, and 1.4 GHz) radio surveys. This multifrequency, multiband information will be exploited to get a comprehensive view of star formation and active galactic nucleus activities in the high-redshift Universe from a radio perspective. In this paper, we present novel 1.4 GHz mosaic observations obtained with the Westerbork Synthesis Radio Telescope. With an area coverage of 6.6 deg^2, this is the largest survey reaching an rms noise of 11 μJy beam^{-1}. In this paper, we present the source catalogue (∼6000 sources with flux densities $S \gtrsim 55$ μJy (5σ), and we discuss the 1.4 GHz source counts derived from it. Our source counts provide very robust statistics in the flux range $0.1 < S < 1$ mJy, and are in excellent agreement with other robust determinations obtained at lower and higher flux densities. A clear excess is found with respect to the counts predicted by the semi-empirical radio sky simulations developed in the framework of the Square Kilometre Array Simulated Skies project. A preliminary analysis of the identified (and classified) sources suggests this excess is to be ascribed to star-forming galaxies, which seem to show a steeper evolution than predicted.

Key words: catalogues – surveys – galaxies: evolution – radio continuum: galaxies.

1 INTRODUCTION

After many years of extensive multiband follow-up studies, it is now established that the sub-mJy population has a composite nature. Radio-loud (RL) active galactic nuclei (AGNs) remain largely dominant down to flux densities of 400–500 μJy (e.g. Mignano et al. 2008), while star-forming galaxies (SFGs) become the dominant population below ∼100 μJy (e.g. Simpson et al. 2006; Seymour et al. 2008; Smolčić et al. 2008). More recently, it has been shown that a significant fraction of the sources below 100 μJy show signatures of AGN activity at non-radio wavelengths (e.g. Seyfert galaxies or QSO). These AGNs are often referred to in the literature as radio-quiet (RQ) AGN (see e.g. Padovani et al. 2009, 2011, 2015; Bonzini et al. 2013), because the vast majority of them do not display large-scale jets or lobes. It is worth noting that these systems are typically radiatively efficient AGNs, characterized by high accretion rates (≳1per cent), while the low-luminosity RL AGN population detected at sub-mJy fluxes is largely made of systems hosted by early-type galaxies (Mignano et al. 2008), likely characterized by radiatively inefficient, low accretion rates (<< 1 per cent). In other words, a classification based on radio loudness (despite not being

★ E-mail: prandoni@ira.inaf.it

fully appropriate for faint radio-selected AGNs[1]) implies, at least in a statistical sense, a more profound distinction between fundamental AGN classes (for a comprehensive review on AGN types and properties we refer to Heckman & Best 2014).

The presence of large numbers of AGN-related sources at sub-mJy/μJy radio flux densities has given a new interesting scientific perspective to deep radio surveys, as they provide a powerful dust/gas-obscuration-free tool to get a global census of both star formation and AGN activity (and related AGN feedback) up to very high redshift and down to the RQ AGN regime (see Padovani 2016 for a comprehensive review). However several uncertainties remain due to observational issues and limitations. First the radio source counts show a large scatter below ∼1 mJy, resulting in a large uncertainty on the actual radio source number density at sub-mJy flux density levels. This scatter can be largely ascribed to cosmic variance effects (Heywood, Jarvis & Condon 2013), but may also be due, at least in some cases, to survey systematics (see e.g. Condon et al. 2012, and discussion in Section 7). Secondly, for a full and robust characterization of the faint radio population the availability of deep multiwavelength ancillary data sets is essential, but typically limited to very small regions of the sky. Mid- and far-infrared (IR) data, as well as deep X-ray information, for example, has proved to be crucial to reliably separate SFGs from RQ AGNs (see e.g. Bonzini et al. 2013, 2015). When available, optical/near-IR spectroscopy is of extreme value, as it provides source redshifts and, if of sufficient quality, a very reliable classification of the host galaxies (SFGs, Seyferts, QSO, etc.), through the analysis of line profiles (broad versus narrow) and line ratios (see e.g. the diagnostic diagrams introduced by Baldwin, Phillips & Terlevich 1981 and later revised by Veilleux & Osterbrock 1987). Alternatively, multiband optical/IR photometry can be used: host galaxies can be classified through their colours and/or spectral energy distributions (SEDs), and stellar masses and photometric estimates of the source redshifts can be derived (several statistical methods and tools are presented in the literature; for a recent application to deep radio continuum surveys, see Duncan et al. 2018a,b).

Finally, the origin of the radio emission in RQ AGNs is currently hotly debated. Most radio-selected RQ AGNs are characterized by compact sizes, i.e. they are unresolved or barely resolved at a few arcsec scale, which is similar to the host galaxy size. RQ AGNs have also been found to share properties with SFGs. They have similar radio spectra and luminosities (Bonzini et al. 2013, 2015); their radio luminosity functions show similar evolutionary trends (Padovani et al. 2011); their host galaxies have similar colours, optical morphologies, and stellar masses (Bonzini et al. 2013). For all these reasons, it was concluded that the radio emission in RQ AGNs is triggered by star formation (Padovani et al. 2011; Bonzini et al. 2013, 2015; Ocran et al. 2017). On the other hand, high-resolution radio follow ups of RQ AGN samples with Very Long Baseline Interferometry arrays have shown that a significant fraction of RQ AGNs (20–40 per cent, depending on the sample) contain AGN cores that contribute significantly (50 per cent or more) to the total radio emission (Maini et al. 2016; Herrera Ruiz et al. 2016, 2017). A different approach was followed by Delvecchio et al. (2017) in the framework of the VLA COSMOS 3 GHz Project. To identify possible AGN contributions, they first exploited the dense multiband information in the COSMOS field to derive accurate star formation rates (SFRs) via SED fitting; then they analysed the ratio between the 1.4 GHz radio luminosity and the SFR for each source. This resulted in ∼30 per cent of the sources with AGN signatures at non-radio wavelengths displaying a significant ($>3\sigma$) radio excess. It is worth noticing that radio selection does not seem to play a major role here. Controversial results arise also from investigations of optically selected QSOs, with authors claiming a pure star formation origin of their radio emission (Kimball et al. 2011; Condon et al. 2013), and others providing evidence of the presence of a radio luminosity excess with respect to SFGs of similar masses (White et al. 2015). Such an excess appears to be correlated with the optical luminosity (White et al. 2017).

The most likely scenario is that RQ AGN are composite systems where star formation and AGN triggered radio emission can coexist, over a wide range of relative contributions. This scenario is supported by the recent modelling work of Mancuso et al. (2017), who showed that the observed radio counts can be very well reproduced by a three-component population (SFGs, RL and RQ AGNs), where RQ AGNs are the sum of two sub-components: one dominated by star formation (so-called radio silent), and the other by AGN-triggered radio emission.

In order to overcome the aforementioned issues about cosmic variance and limited multiband information, deep radio samples over wide areas ($>>1$ deg^2) are needed, in regions where deep multiband ancillary data are available. This is a pre-requisite to get robust estimations of the sub-mJy radio source number density and of the fractional contribution of each class of sources as a function of cosmic time in representative volumes of the Universe (i.e. not biased by cosmic variance). At the same time, wide-area surveys allow us to probe AGNs and/or star formation activities in a variety of different environments. Additional important information may come from multifrequency radio coverage: radio spectra may help to constrain the origin of the radio emission in the observed sources and to understand its link to the host galaxy bolometric emission. This is especially true if high-resolution radio data are available and source structures can be inferred. SFGs typically have a *steep* radio spectral index ($\alpha \sim -0.7/-0.8$, where $S \propto \nu^{\alpha}$), with a relatively small dispersion (± 0.24, Condon 1992). Radio spectral index studies combined with source structure information (radio jets and lobes) may thus help to disentangle star forming from steep-spectrum radio galaxy populations. A *flat* ($\alpha > -0.5$) radio spectral index can identify core-dominated AGNs (Blundell & Kuncic 2007) and GHz-peaked sources (Gopal-Krishna, Patnaik & Steppe 1983; O'Dea 1998; Snellen et al. 2000). Ultra-steep radio spectra ($\alpha < -1$; Röttgering et al. 1994; Chambers et al. 1996; Jarvis et al. 2001) are a typical feature of high-redshift ($z >>2$) radio galaxies.

The Lockman Hole (LH, Lockman, Jahoda & McCammon 1986) is one of the best studied extragalactic regions of the sky (see Section 2 for a comprehensive summary of the available multiband coverage in this region). Given its high declination ($\sim +58^{\circ}$), the LH is also best suited for deep, high-resolution, high-fidelity imaging with the LOw-Frequency ARray (LOFAR).

The LH Project is an international collaboration aimed at extending the multiband information available in the LH region, through novel multifrequency radio surveys down to 60–150 MHz, a frequency domain that is now accessible for wide-area deep fields thanks to the combination of field of view, sensitivity, and spatial resolution of LOFAR. This information, together with the available ancillary data, will allow us to get robust observational constraints on the faint extragalactic radio sky, in preparation for

[1]A detailed discussion of AGN classification in view of the latest results from deep radio surveys, is presented in Padovani (2017), who proposes to update the terms RL/RQ AGNs into jetted/non-jetted AGNs, based on the presence/lack of strong relativistic jets.

next-generation continuum extragalactic surveys with the Australia Square Kilometre Array Pathfinder (ASKAP; Johnston et al. 2007), MeerKat (Booth & Jonas 2012), and ultimately the Square Kilometre Array (SKA).

This paper presents a Westerbork (WSRT) 1.4 GHz mosaic covering ∼6.6 deg^2 down to 11 μ beam^{-1} rms and the source catalogue extracted from it. The 345 MHz follow-up, again obtained with the WSRT, is presented in a following paper (Prandoni et al., in preparation), while the first LOFAR observations of this region are presented in Mahony et al. (2016).

This paper is organized as follows. Section 2 gives an overview of the multiwavelength data available for the LH region. In Sections 3, we describe the WSRT 1.4 GHz observations, the related data reduction and the analysis performed to characterize the noise properties of the final mosaic. In Section 4, we describe the method used to extract the sources and the final catalogue obtained. In Sections 5 and 6, we provide estimates of the source parameters' errors and we analyse possible systematic effects. In Section 7, we present the source counts derived from the present catalogue and we discuss them in comparison with other existing source counts obtained from wide-area 1.4 GHz surveys. In Section 8, we assess the contribution of each class of sources to our overall radio source counts, based on a preliminary analysis of the radio source optical/IR properties, and we compare it to existing modelling predictions. In Section 9, we summarize our main results.

2 MULTIWAVELENGTH COVERAGE OF THE LOCKMAN HOLE REGION

The LH is the region of lowest H I column density in the sky. Its low-IR background (0.38 MJy sr^{-1} at 100 μm; Lonsdale et al. 2003) makes this region particularly well suited for deep-IR observations. The *Spitzer Space Telescope* (Werner et al. 2004) observed ∼12 deg^2 of the LH region in 2004 as part of the Spitzer Wide-area Infrared Extragalactic survey (SWIRE; Lonsdale et al. 2003). Observations were performed using the Infrared Array Camera (IRAC; Fazio et al. 2004) operating at 3.6, 4.5, 5.8, and 8 μm, and the Multiband Imaging Photometer for Spitzer (Rieke et al. 2004) at 24, 70, and 160 μm. Deeper, confusion-limited observations at 3.6 and 4.5 μm were obtained over ∼4 deg^2 during the warm mission of *Spitzer* as part of the Spitzer Extragalactic Representative Volume Survey (SERVS, Mauduit et al. 2012). In addition about 16 deg^2 overlapping with the SWIRE survey of the LH have been targeted by the *Herschel Space Observatory* with the Photoconductor Array Camera and Spectrometer (100 and 160 μm) and the Spectral and Photometric Imaging REceiver (250, 350, and 500 μm) as part of the Herschel Multi-tiered Extragalactic Survey (Oliver et al. 2012).

A great deal of complementary data have been taken on the LH at other wavelengths in order to exploit the availability of sensitive IR observations, including *GALEX* GR6Plus7 ultraviolet (UV) photometry (Martin et al. 2005), Sloane Digital Sky Survey (SDSS) DR14 optical spectroscopy and photometry in the *ugriz* bands to a depth of ∼22 mag (Abolfathi et al. 2018), INT Wide Field Camera optical photometry (u, g, r, i, z down to AB magnitudes 23.9, 24.5, 24.0, 23.3, 22.0 respectively; Gonzáles-Solares et al. 2011) and UK Infrared Deep Sky Survey Deep Extragalactic Survey (UKIDSS DXS) DR10Plus photometry in the J and K bands, with a sensitivity of K ∼ 21–21.5 mag (Vega; Lawrence et al. 2007). There are existing near-IR data across the region from the Two Micron All Sky Survey (Beichman et al. 2003) to J, H, and Ks band magnitudes of 17.8, 16.5, and 16.0. A photometric redshift catalogue containing 229 238 galaxies and quasars within the LH has been constructed from band-merged data (Rowan-Robinson et al. 2008; but see Rowan-Robinson et al. 2013 for the latest version of the SWIRE photometric redshift catalogue, including photometric redshifts and SED models based on optical, near-IR, and *Spitzer* photometry). Deep surveys within the LH region have been undertaken with the Submillimetre Common-User Bolometer Array (Holland et al. 1999) at 850 μm (Coppin et al. 2006), and with the X-ray satellites *ROSAT* (Hasinger et al. 1998), *XMM–Newton* (Hasinger et al. 2001; Mainieri et al. 2002; Brunner et al. 2008), and *Chandra* (Polletta et al. 2006).

A variety of radio surveys cover limited areas within the LH region, in coincidence with the two deep X-ray fields (highlighted in Fig. 1). The first of these was by de Ruiter et al. (1997), who observed an area of 0.35 deg^2 at 1.4 GHz centred on the *ROSAT*/*XMM* pointing (RA = 10:52:09; Dec.=+57:21:34, J2000), using the Very Large Array (VLA) in C-configuration, with an rms noise level of 30−55 μJy beam^{-1}. A similar deep observation was carried out by Ciliegi et al. (2003), who observed an 0.087 deg^2 region at 4.89 GHz using the VLA in C-configuration, with an rms noise level of 11 μJy beam^{-1}. More recently, Biggs & Ivison (2006) observed a 320 arcmin^2 area, using the VLA at 1.4 GHz operating in the A- and B-configurations, and with an rms noise level of 4.6 μJy beam^{-1}. VLA B-configuration 1.4 GHz observations of a larger region (three overlapping VLA pointings) were performed by Ibar et al. (2009), reaching an rms noise of ∼6 μJy beam^{-1} in the central 100 arcmin^2 area. These observations were matched with 610 MHz Giant Metrewave Radio Telescope (GMRT) observations down to an rms noise of ∼15 μJy beam^{-1}. Less sensitive GMRT 610 MHz observations of a much larger area were carried out by Garn et al. (2008a,b), covering ∼5 deg^2 down to an rms noise of ∼60 μJy. This survey was later extended to ∼13 deg^2 (Garn et al. 2010). Two fields of the 10C 15 GHz survey (AMI consortium, 2011; Whittam et al. 2013) overlap with the LH region, for a total of ∼4.6 deg^2. The rms noise levels of ∼50−100 μJy were reached at a spatial resolution is 30 arcsec. The deepest 1.4 GHz observations to date (rms noise of ∼2.7 μJy beam^{-1} were performed by Owen & Morrison (2008) at the location of the *Chandra* deep pointing (RA = 10:46, Dec.=+59:00, J2000). This was later matched with very sensitive VLA (C-configuration) 324.5 MHz observations down to an rms noise of ∼70 μJy beam^{-1} in the central part (Owen et al. 2009). This field (also known as Lockman North) has been recently the target of wide-band 3 GHz observations with the upgraded Karl Jansky VLA, reaching an rms noise level of 1.01 μJy beam^{-1} (Condon et al. 2012; Vernstrom et al. 2014, 2016a,b). The Faint Images of the Radio Sky at Twenty cm (FIRST; Becker, White & Helfand 1995) and NRAO VLA Sky Survey (NVSS; Condon et al. 1998) surveys both cover the entire region at 1.4 GHz, but only to relatively shallow noise levels of 150 and 450 μJy beam^{-1}, respectively.

Finally, as part of the LH Project, the field has been imaged with WSRT at 350 MHz down to the confusion limit (∼0.5 mJy rms; Prandoni et al. in preparation), and with LOFAR at 150 MHz (∼160 μJy rms; Mahony et al. 2016). Deeper 150 MHz LOFAR observations are ongoing (Mandal et al. in preparation). Mahony et al. (2016) present a multifrequency study of the radio sources in the field, based on most of the aforementioned radio observations, including the catalogue presented here. The combination of LOFAR 150 MHz and WSRT 1.4 GHz data, resulted in a sample of 1302 matched sources (see Mahony et al. 2016, for more details).

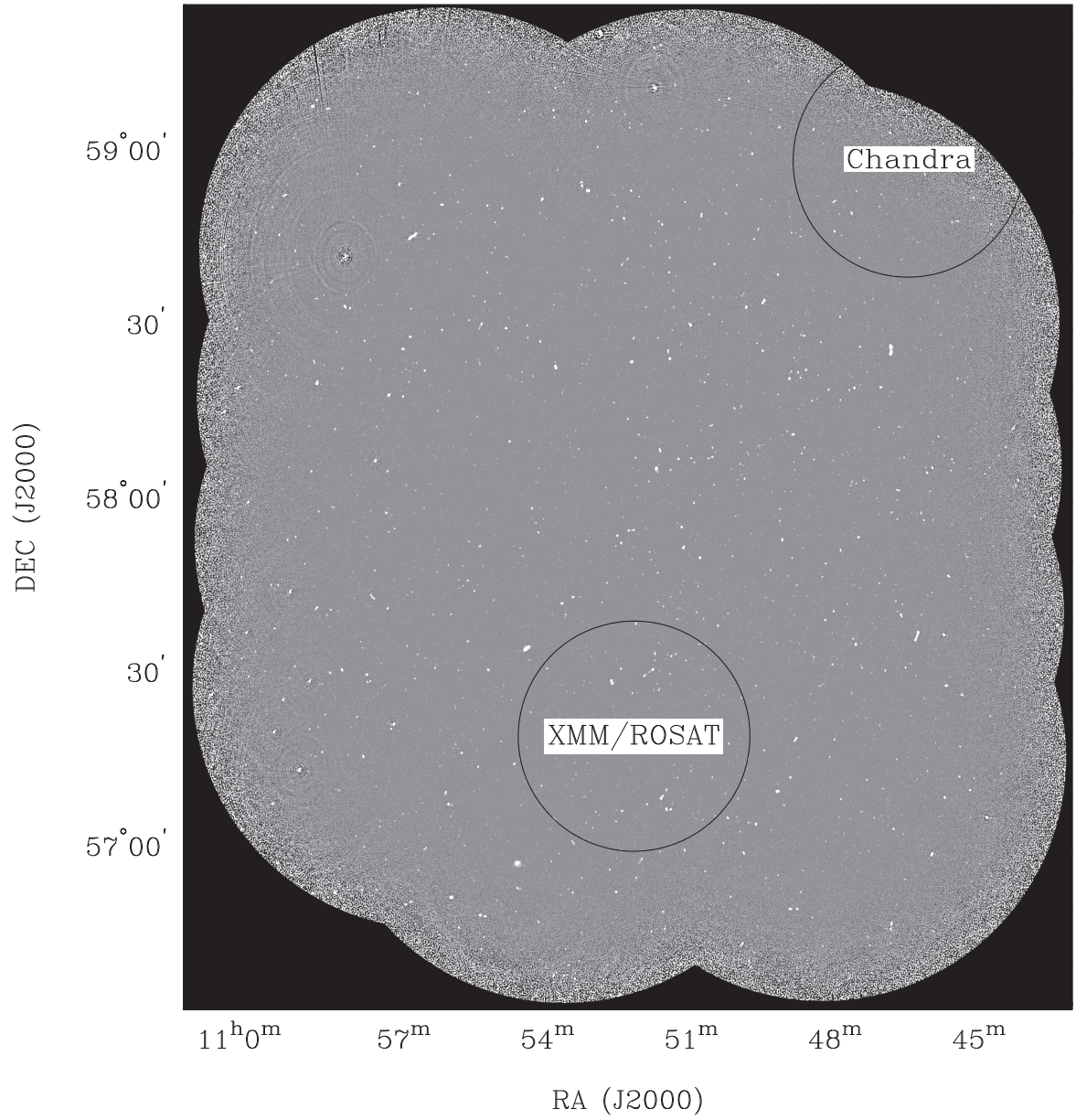

Figure 1. The WSRT 1.4 GHz mosaic: 16 overlapping pointings, with spacing of 22 arcmin in RA and 25 arcmin in Dec. Highlighted are the two locations of the deep X-ray fields, where most existing deep radio observations have been taken (see text for more details).

3 THE NEW 1.4 GHz MOSAIC

We observed the LH region with the WSRT at 1.4 GHz, in the period 2006 December–2007 June. The observations covered an area of ∼6.6 deg^2 (mostly overlapping the *Spitzer* and *Herschel* surveys), through overlapping pointings. A good compromise between uniform sensitivity and observing efficiency is generally obtained with a mosaic pattern where pointing spacings, s, are ≈FWHP', where FWHP'=FWHP/$\sqrt{2}$, and FWHP is the full width at half-power of the primary beam (see Prandoni et al. 2000a). For our particular case FWHP∼36 arcmin, and FWHP'∼25.46 arcmin. From noise simulations, we got 5 per cent noise variations with $s = 0.85$ FWHP' (=22 arcmin) and 10 per cent variations with $s =$ FWHP'. We then decided to cover the 6.6 deg^2 area with 16 overlapping pointings, with spacing of 22 arcmin in RA and 25 arcmin in Dec. Each field was observed for 12 h. The primary calibrator (3C 48) was observed for 15 min at the beginning of each 12 h run, and the secondary calibrator (J1035+5628), unresolved on VLBA scale, was observed for 3 min every hour. The data were recorded in 512 channels, organized in eight 20 MHz sub-bands, 64 channels each. The channel width is 312 KHz, and the total bandwidth is 160 MHz.

For the data reduction, we used the MULTICHANNEL IMAGE RECONSTRUCTION, IMAGE ANALYSIS AND DISPLAY(MIRIAD) software package (Sault et al.1995). Each field was calibrated and imaged separately. Imaging and deconvolution was performed in multi-frequency synthesis mode, taking into proper account the spectral variation of the dirty beam over the image during the cleaning process (MRIAD task MFCLEAN). Each field was cleaned to a distance of 50 arcmin from the phase centre (i.e. down to about the zero-point primary beam width) in order to deconvolve all the sources in the field. All the images were produced using uniform weighting to get the maximum spatial resolution. Subsequently, we combined

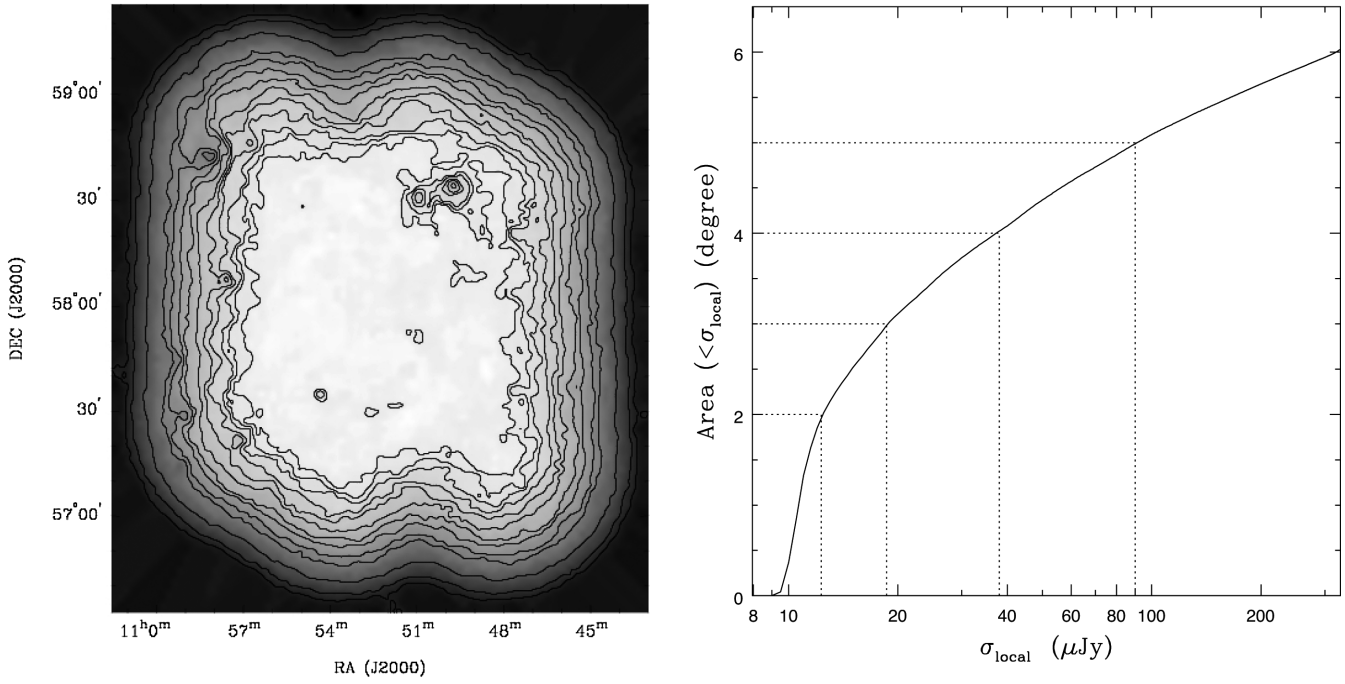

Figure 2. Left: noise map. Contours refer to 1.1, 1.2, 1.3, 1.5, 1.7, 2, 2.5, 3, 4, 5, 10, 20, and 30 multiples of the noise centre value (11 μJy). Right: visibility area of the WSRT 1.4 GHz mosaic. Cumulative fraction of the total area of the noise map characterized by a measured noise lower than a given value. Dotted lines indicate the maximum noise value measured over an area of 2, 3, 4 and 5 deg^2 .

together all the images to create a single primary beam corrected mosaic (pixel size =2 arcsec). The synthesized beam is 11 arcsec × 9 arcsec, with position angle PA = 0°. The resulting 1.4 GHz mosaic, centred at RA = 10:52:16.6; Dec.=+58:01:15 (J2000), is shown in Fig. 1.

3.1 Noise map

To investigate the noise characteristics of our 1.4 GHz image, we constructed a noise map with the software SExtractor (Bertin & Arnouts 1996). Although SExtractor was originally developed for the analysis of optical data, it is widely used for noise analysis of radio images as well (see e.g. Bondi et al. 2003; Huynh et al. 2005; Prandoni et al. 2006). SExtractor initially estimates the local background in each mesh from the pixel data. Then the local background histogram is clipped iteratively until convergence is reached at $\pm 3\sigma$ around its median. The choice of mesh size is very important. When it is too small, the background tends to be overestimated due to the presence of real sources. When it is too large, any small-scale variation of the background is washed out. A mesh size of 50 × 50 pixel (approximately 10 × 10 beams), was found to be appropriate for our case (see also discussion in Section 4). However, it should be noted that border effects make the determination of the local noise less reliable in the outermost regions of the mosaic.

The obtained noise map is shown in Fig. 2 (left-hand panel). The rms was found to be approximately uniform (noise variations < 10 per cent) over the central region, with a value of about 11 μJy. Then, it radially increases up to ∼500 μJy at the very border of the mosaic. This is in agreement with the expectations, as better discussed in Section 4. Sub-regions characterized by noise values higher than the expected ones are found to correspond to very bright sources, due to dynamic range limits introduced by residual phase errors. In Fig. 2 (right-hand panel), the total area of the noise map characterized by noise measurements lower than a given value is plotted. The inner ∼2 deg^2 region is characterized by a noise increment ≤ 10 per cent (noise values ≤12 μJy). Noise increments to 18, 38, and 90 μJy are measured over the inner 3, 4, and 5 deg^2 respectively (see dotted lines in right-hand panel of Fig. 2). We notice that border effects are present in the very external mosaic region characterized by noise values larger than ∼330 μJy (i.e. 30 × 11μJy, see last contour in Fig. 2, left-hand panel).

4 THE 1.4 GHz SOURCE CATALOGUE

The source extraction was performed over the entire mosaic (up to rms noise values of ∼500 μJy), even though the source catalogue should be considered reliable and complete only up to local noise values of 330 μJy. To take into proper account both local and radial noise variations, sources were extracted from a signal-to-noise map produced by dividing the mosaic by its noise map. A preliminary list of more than 6000 sources with S/N ≥ 5 was derived using the MIRID task IMSAD.

All the source candidates were visually inspected. The goodness of Gaussian fit parameters was checked following Prandoni et al. (2000b, see their section 2). Typical fitting problems arise whenever:

(i) Sources are fitted by IMSAD with a single Gaussian but are better described by two or more Gaussian;
(ii) Sources are extended and are not well described by a Gaussian fit.

In the first case, sources were re-fitted using multiple Gaussian components. The number of successfully split sources is 74 in total (62 in two components, 10 in three components, and 2 in four components). In the second case (134 non-Gaussian sources or source components), integrated flux densities were measured by summing

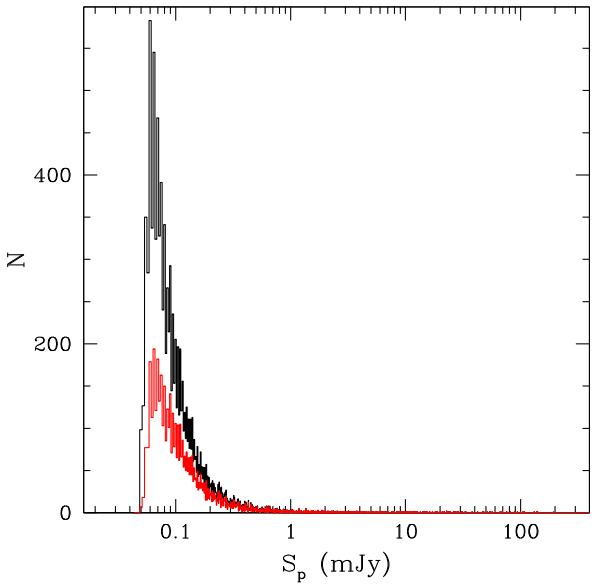

Figure 3. Peak flux density distribution of the radio sources (or source components) before (red) and after (black) taking into proper account the noise variations along the mosaic. In the latter case, the source number is weighted for the reciprocal of the visibility area shown in Fig. 2 (right-hand panel), where we assume $S_{\rm peak} > 5\sigma_{\rm local}$.

all the pixels above a reference 3σ threshold, using the MIRIAD task CGCURS, which also gives the position and flux density of the source peak. Non-Gaussian sources are flagged as '*E*' in the catalogue. In a few additional cases, Gaussian fits were able to provide good values for positions and peak flux densities, but did fail in determining the integrated flux densities. This happens typically at low signal-to-noise values. Gaussian sources with a poor determination of the integrated flux are flagged in the catalogue as '*G*∗'. We also noticed that in a few cases our procedure (IMSAD+SExtractor) failed to detect very extended low-surface brightness sources. This is due to the fact that the source itself can affect the local noise computation, producing a too high detection threshold ($5\sigma_{\rm local}$). The few missing large low-surface brightness sources were easily recognized by eye, and added to the catalogue.

Once the final source list was produced, we computed the local noise, $\sigma_{\rm local}$, around each source (measured in 50 × 50 pixel regions centred at each source position in the noise map) and used it to transform the peak and integrated flux densities from S/N units to mJy units.

After accounting for the splitting in multiple Gaussian components the catalogue lists 6194 sources (or sources components). The peak flux distribution of our sources is shown in Fig. 3 before (red histogram) and after (black histogram) taking into proper account the noise variations along the mosaic. Once corrected for the source visibility area (see Fig. 2, right-hand panel), the peak flux distribution gets narrower, showing a steeper increase going to lower flux densities. However, some incompleteness can still be seen in the lowest flux density bins. This incompleteness is the expected effect of the noise at the source extraction threshold. Due to its Gaussian distribution, whenever a source falls on a noise dip, either the source flux is underestimated or the source goes undetected. This produces incompleteness in the faintest bins. As a consequence, the measured fluxes of detected sources are biased toward higher values in the incomplete bins, because only sources that fall on noise peaks have been detected and measured. As demonstrated through

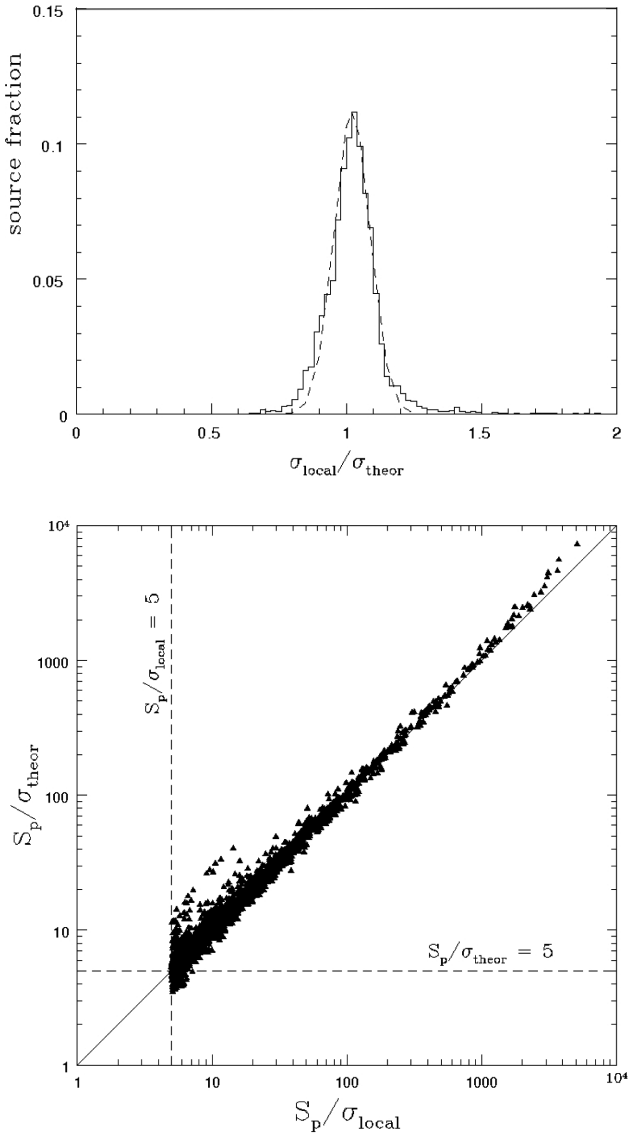

Figure 4. Top: local to expected noise ratio distribution as measured in a 50 × 50 pixel box around each source. The distribution is well fitted by a Gaussian with FWHM = 0.137 and peak position equal to 1.02 (dashed line). Bottom: signal-to-noise ratios as measured using either $\sigma_{\rm local}$ or $\sigma_{\rm theor}$. Vertical and horizontal dashed lines indicate the 5σ cut-off for the two signal-to-noise measurements, respectively.

Monte Carlo simulations in Prandoni et al. (2000b), incompleteness can be as high as 50 per cent at the 5σ threshold, reducing down to 15 per cent at 6σ, and to 2 per cent at 7σ. Correspondingly, source fluxes are boosted by a factor of 18 per cent at 5σ, 10 per cent at 6σ, and 6 per cent at 7σ. However, such incompleteness effects can be counterbalanced (at least partially – the extent actually depends on the shape of the source counts) by the fact that sources below the detection threshold can be pushed above it when they sit on a noise peak.

4.1 Noise analysis

To better investigate the local noise ($\sigma_{\rm local}$) distribution, we compared it with the expected noise ($\sigma_{\rm theor}$), defined as the average noise value measured within a 50 × 50 pixel box centred at the same

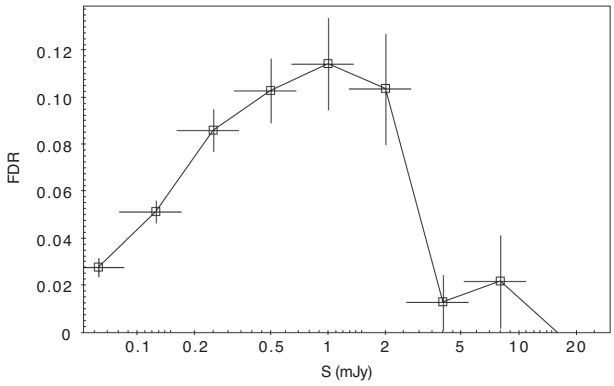

Figure 5. FDR as a function of integrated flux density.

position in the so-called *sensitivity map*, which is a map of the expected noise, based on the integration time spent on each observed field, and on the complex primary beam response obtained when linearly combining all the fields in the final mosaic. As shown in Fig. 4 (top panel), the local noise does not generally shows significant systematic departures from the expected rms value: the distribution can be described fairly well by a Gaussian with FWHM = 0.137 and a peak position equal to 1.02 (dashed line). Also compared are the signal-to-noise ratios defined, for each source, using either $\sigma_{\rm local}$ or $\sigma_{\rm theor}$ (Fig. 4, bottom panel). The two measured signal-to-noise ratios mostly agree with each other, although a number of significant departures are evident for the faintest and brightest sources. This is due to the presence of some residual areas where the noise is not random due to systematic effects (typically phase errors around bright sources).

To quantify the effect of non-Gaussian noise on our source catalogue, we quantified the number of possible spurious detections in the following way. By assuming that negative and positive noise spikes have a similar distribution, we ran IMSAD on the negative mosaic map (i.e. the map multiplied by -1), with the same input parameters used to extract the source catalogue. We found 356 components above the 5σ threshold, within the completeness area of the catalogue (local noise $<$330 μJy), corresponding to a fraction of 5.8 per cent. The false detection rate (FDR; i.e. the ratio between the number of spurious components and the number of components in the catalogue) as a function of total flux is shown in Fig. 5. The FDR peaks around $\sim$0.5−2 mJy, where we can expect a contamination from artefacts $\gtrsim$10 per cent. Sources which from visual inspection appear to be likely noise peak are flagged as '*n*' in the catalogue.

4.2 Bandwidth smearing

Bandwidth smearing, the radio analogue of optical chromatic aberration, is a well-known effect caused by the finite width of the receiver channels. It reduces the peak flux density of a source while correspondingly increasing the apparent source size in the radial direction such that the total integrated flux density is conserved. The amount of smearing is proportional to the distance from the phase centre and the channel width (or passband) of the data. Assuming a Gaussian beam and passband (see Condon et al. 1998), we find that in our particular case the expected peak flux density attenuation at the maximum distance from the phase centre (50 arcmin; see Section 3) is $S_{\rm peak}/S^0_{\rm peak} = 0.999$, where $S^0_{\rm peak}$ represents the un-smeared source peak flux density. It is therefore clear that bandwidth smearing is not an issue for our source catalogue.

4.3 Deconvolution

The ratio of the integrated flux to the peak flux is a direct measure of the extent of a radio source:

$$S_{\rm tot}/S_{\rm peak} = \theta_{\rm maj}\theta_{\rm min}/b_{\rm maj}b_{\rm min} \quad (1)$$

where $\theta_{\rm maj}$ and $\theta_{\rm min}$ are the source FWHM axes and $b_{\rm maj}$ and $b_{\rm min}$ are the synthesized beam FWHM axes. The flux ratio can therefore be used to discriminate between extended (larger than the beam) and point-like sources. In Fig. 6, we have plotted the flux ratio $S_{\rm tot}/S_{\rm peak}$ as a function of the signal-to-noise ratio for all the sources (or source components) in our catalogue.

The flux density ratio has a skewed distribution, with a tail towards high flux ratios due to extended sources. To establish a criterion for classifying extended sources, errors in the flux measurement have to be taken into account, since such errors can introduce an intrinsic spread even in case of points sources. We have determined the 1σ error fluctuation of the ratio $S_{\rm tot}/S_{\rm peak}$ as a function of the signal-to-noise ratio using the Condon (1997) equations of error propagation derived for two-dimensional elliptical Gaussian fits of point sources in presence of Gaussian noise (see equations 4–6 in Section 5). We find an envelope function that can be characterized by the equation:

$$S_{\rm tot}/S_{\rm peak} = 1 + 1.4\left(\frac{S_{\rm peak}}{\sigma_{\rm local}}\right)^{-1} \quad (2)$$

(see dashed line in Fig. 6).

We have then considered as truly resolved only those sources laying above such envelope. From this analysis, we found that 2548 sources (or source components) in the catalogue are unresolved (red dots in Fig. 6). Another 599 are resolved only in the major axis direction. In total, we have 3047 fully resolved sources ($\sim$50 per cent of the sample). The deconvolved angular sizes of unresolved sources are set to zero in the catalogue. For a size distribution of the sources, we refer to Fig. 10. It is worth noting that the fraction of unresolved/resolved sources in a radio catalogue very much depends on the criteria adopted to make this distinction. Assuming a more conservative envelope function that accounts for 2σ $S_{\rm tot}/S_{\rm peak}$ fluctuations, the fraction of resolved sources would get down to 27 per cent.

4.4 Multiple-component sources

Radio sources associated with radio galaxies can be made up of a nucleus with hotspots along, or at the end of, one or two jets. The individual components of a single source are often cataloged separately by Gaussian fitting routines, so a method must be devised to identify multiple components as belonging to a single source.When jets are detected it is relatively easy to recognize the components belonging to the same source, and indeed through visual inspection we were able to recognize such cases (see discussion above). More difficult is the case when only lobes are detected (double-component sources), and no sign of connecting jets is present. To recognize such double-component sources, we applied the statistical technique of Magliocchetti et al. (1998), later modified by Huynh et al. (2005), where the sum of the fluxes of each nearest neighbor pair ($S_{\rm sum}$) versus their separation (d) is analysed (see Fig. 7). The high density of points to the lower right of the $S_{\rm sum} - d$ plane is to be ascribed to the

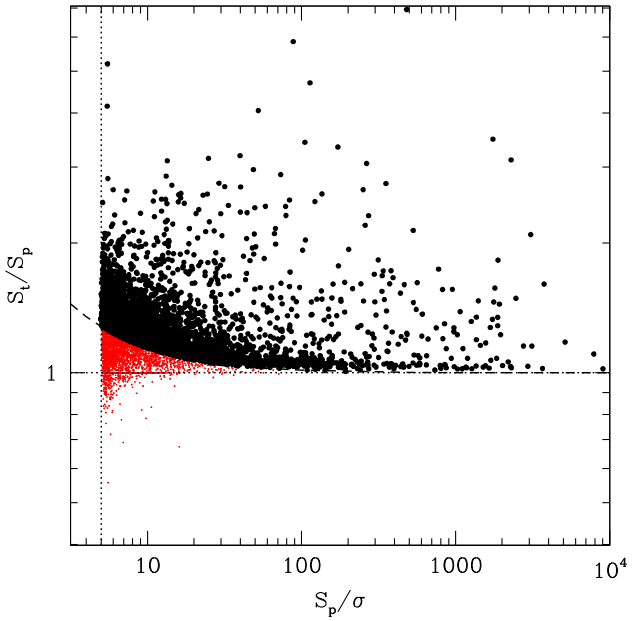

Figure 6. Integrated to peak flux ratio as a function of the source signal-to-noise ratio. Lines indicate the S/N = 5 cut-off adopted in the source catalogue extraction (dotted), the locus $S_t/S_p = 1$ (solid), and the envelop function defined by equation (2) (dashed). Red dots correspond to unresolved sources; and black filled circles correspond to resolved or partially resolved sources (i.e. those sources that are resolved only along the major axis).

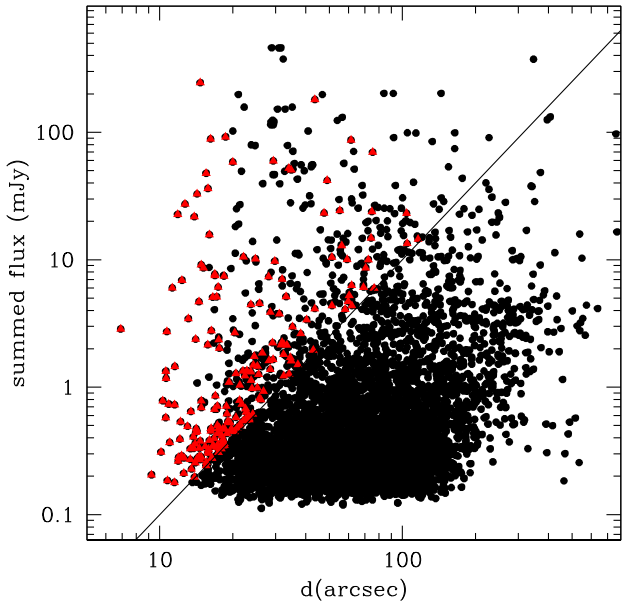

Figure 7. Sum of the flux densities of nearest neighbour pairs plotted against their separation. Source pairs that lie above the solid line and have flux densities that differ by less than a factor of 4 are considered as double source candidates (see red filled triangles).

general population of single-component sources. Following Huynh et al. (2005), a maximum allowed separation for double-component sources is then applied as a function of the summed flux density, as follows:

$$d_{\max} = 100(S_{\rm sum}/10)^{0.5} \quad (3)$$

where $S_{\rm sum}$ is given in mJy and $d_{\max}$ in arcsec. This maximum separation is shown as a solid line in Fig. 7. This procedure proves to be more successful than distance-only-based criteria for very deep surveys like ours, where random pairs can be found even at very small separations. In fact a maximum separation varying with summed flux allows to consider *faint* pairs, which are likely to be found by chance, as single sources even when at very small separations; at the same time it allows to include among real pairs *bright* sources at large separation.

Since flux densities of components of real double sources are typically similar, a second constraint was then applied to restrict the matched pairs to real physically associated sources. Following Huynh et al. (2005), we consider pairs as really physically associated only if their flux densities differ by a factor of less than 4. Sources that meet this further requirement are shown in Fig. 7 as red filled triangles. From this analysis, we could identify 155 additional double source candidates. All such sources were again visually inspected, and 46 were discarded as they are clearly random associations (mainly based on component morphology and pair alignment considerations). The remaining 109 pairs are included as double sources and flagged '*M*' in this release of the catalogue. In the future, these sources will be further investigated (and possibly confirmed as multiple) through inspection of the deep optical/IR catalogues and images covering the LH region. This will allow us to identify the host galaxy possibly associated to (multiple) radio sources.

4.5 Catalogue format

The final catalogue lists 5997 sources, including 183 multiple-component sources. Most (90 per cent) are sub-mJy sources. The full radio catalogue is available in electronic form. A sample is shown in Table 1.

For multiple sources, we list all the components (labelled 'A', 'B', etc.) preceded by a line (flagged '*M*') giving the position of the radio centroid, the total flux density, and the overall angular size of the source. Source positions have been defined as the flux-weighted average position of the components (source centroid). For sources with more than two components the centroid position has been replaced with the core position whenever the core is clearly recognizable. Total source flux densities are computed by summing all the component integrated fluxes. Multiple source angular sizes are defined as largest angular sizes (*las*), i.e. the maximum distance between the source components.

5 ERRORS IN SOURCE PARAMETERS

Parameter uncertainties are the quadratic sum of two independent terms: the calibration errors, which dominate at high signal-to-noise ratios, and the internal errors, due to the presence of noise in the maps. The latter dominate at low signal-to-noise ratios. For an estimate of the internal errors of the source parameters, we refer to Condon's master equations (Condon 1997), which provide error estimates for elliptical Gaussian fitting procedures. Such equations already proved to be adequate to describe the measured internal errors for other similar deep 1.4 GHz radio catalogues, obtained with the same detection and fitting algorithm (IMSAD) applied to radio mosaics (see e.g. Prandoni et al. 2000b). Applying Condon's master equation to our radio survey, we derived the relations which describe 1σ internal errors for flux density and source axis fitting

Table 1. The radio catalogue: sample (the full version is available in electronic form).

IAU name	RA J2000	Dec. J2000	S_{peak} (mJy)	S_{tot} (mJy)	θ_{maj} (arcsec)	θ_{min} (arcsec)	PA (deg)	$d\theta_{maj}$ (arcsec)	$d\theta_{min}$ (arcsec)	dPA (deg)	σ_{local} (mJy)		
LHW J104515+580634	10 45 15.31	+58 06 34.6	1.099	1.323	12.10	9.84	27.4	6.45	0.00	52.9	0.0301	G	
LHW J104515+575711	10 45 15.92	+57 57 11.4	0.321	0.574	18.10	9.78	− 2.5	14.38	3.82	− 3.0	0.0262	G	c
LHW J104517+580737	10 45 17.82	+58 07 37.1	0.281	0.301	11.50	9.20	24.2	0.00	0.00	0.0	0.0295	G	
LHW J104518+571626	10 45 18.41	+57 16 26.7	0.233	0.267	12.80	8.82	16.7	0.00	0.00	0.0	0.0293	G	
LHW J104518+571012	10 45 18.90	+57 10 12.9	0.184	0.236	12.40	10.22	12.6	6.23	4.17	38.8	0.0330	G	
LHW J104519+581742	10 45 19.19	+58 17 42.5	0.151	0.148	10.70	9.03	− 2.8	0.00	0.00	0.0	0.0288	G	
LHW J104519+581044	10 45 19.91	+58 10 44.6	0.157	0.210	13.80	9.58	− 15.2	8.59	2.54	− 24.0	0.0298	G	
LHW J104519+571545	10 45 19.97	+57 15 45.5	0.245	0.282	11.80	9.60	0.4	0.00	0.00	0.0	0.0290	G	
LHW J104520+581224	10 45 20.54	+58 12 24.1	0.345	0.417	11.70	10.17	8.3	5.04	3.60	64.8	0.0291	G	
LHW J104520+583714	10 45 20.60	+58 37 14.8	0.219	0.232	11.80	8.83	1.8	0.00	0.00	0.0	0.0284	G	
LHW J104521+575553	10 45 21.87	+57 55 53.4	0.154	0.221	13.70	10.33	− 24.5	8.80	3.87	− 38.9	0.0264	G	
LHW J104521+575027	10 45 21.90	+57 50 27.8	0.200	0.202	10.70	9.34	14.5	0.00	0.00	0.0	0.0262	G	
LHW J104522+574827	10 45 22.31	+57 48 27.3	12.450	14.829	39.84	23.96	48.1	38.58	21.69	49.2	0.0263	E	m
LHW J104522+572824	10 45 22.44	+57 28 24.6	0.158	0.195	12.80	9.50	− 13.1	0.00	0.00	0.0	0.0281	G	
LHW J104522+582203	10 45 22.54	+58 22 03.9	0.172	0.178	10.50	9.70	2.4	0.00	0.00	0.0	0.0257	G	
LHW J104522+590742	10 45 22.59	+59 07 42.7	2.585	2.421	10.40	8.85	− 13.4	0.00	0.00	0.0	0.3610	G	
LHW J104522+571727	10 45 22.63	+57 17 27.9	0.164	0.177	12.50	8.53	22.7	0.00	0.00	0.0	0.0282	G	
LHW J104523+573057	10 45 23.20	+57 30 57.9	0.347	0.458	13.60	9.56	− 7.2	8.06	3.05	− 12.3	0.0282	G	
LHW J104523+580913	10 45 23.48	+58 09 13.1	0.431	0.634	12.40	11.69	− 18.8	7.64	5.48	− 79.2	0.0288	G	
LHW J104524+582957	10 45 24.00	+58 29 57.5	0.895	0.937	10.90	9.46	− 12.7	3.52	0.00	− 68.5	0.0252	G	
LHW J104524+582610	10 45 24.31	+58 26 10.7	0.183	0.243	14.10	9.33	− 1.6	8.82	2.45	− 2.5	0.0240	G	
LHW J104524+575926	10 45 24.34	+57 59 26.8	0.206	0.234	12.20	9.22	− 23.6	0.00	0.00	0.0	0.0260	G	
LHW J104524+573831	10 45 24.89	+57 38 31.0	0.169	0.156	11.20	8.07	14.6	0.00	0.00	0.0	0.0313	G	n
LHW J104524+570933	10 45 24.92	+57 09 33.1	0.494	0.511	11.30	9.01	0.5	0.00	0.00	0.0	0.0309	G	
LHW J104525+573808	10 45 25.69	+57 38 08.6	0.329	0.441	13.00	10.19	− 34.7	8.19	1.94	− 52.8	0.0315	G	n
LHW J104526+583531	10 45 26.77	+58 35 31.1	0.582	0.788	32.70						0.0242	M	
LHW J104526+583531A	10 45 26.76	+58 35 26.6	0.582	0.620	11.10	9.43	− 3.1	2.93	1.26	− 74.0	0.0242	G	
LHW J104526+583531B	10 45 26.78	+58 35 47.9	0.137	0.168	11.70	10.38	− 4.2	0.00	0.00	0.0	0.0243	G	
LHW J104527+572436	10 45 27.61	+57 24 36.9	0.307	0.390	13.40	9.33	− 16.9	8.00	0.81	− 27.2	0.0247	G	
LHW J104527+564137	10 45 27.84	+56 41 37.2	2.200	2.167	10.90	8.89	1.6	0.00	0.00	0.0	0.4140	G	
LHW J104527+565910	10 45 27.93	+56 59 10.0	0.301	0.268	10.40	8.43	31.6	0.00	0.00	0.0	0.0506	G	
LHW J104528+572928	10 45 28.36	+57 29 28.2	10.521	22.671	40.63						0.0272	M	
LHW J104528+572928A	10 45 27.74	+57 29 28.2	10.521	13.078	11.29	10.90	26.8	6.32	2.09	84.4	0.0272	G	
LHW J104528+572928B	10 45 29.21	+57 29 28.2	7.968	9.593	11.31	10.54	− 23.8	5.84	1.70	− 78.3	0.0270	G	
LHW J104528+575347	10 45 28.45	+57 53 47.5	0.143	0.192	11.70	11.36	32.9	7.12	3.64	84.5	0.0259	G	
LHW J104529+581749	10 45 29.28	+58 17 49.2	0.129	0.159	13.40	9.06	12.8	0.00	0.00	0.0	0.0254	G	
LHW J104529+573817	10 45 29.97	+57 38 17.0	66.508	70.508	11.40	9.21	7.2	3.51	0.69	35.8	0.0303	G	
LHW J104530+581231	10 45 30.47	+58 12 31.6	1.791	1.945	11.40	9.38	4.5	3.37	2.15	38.7	0.0260	G	
LHW J104530+571220	10 45 30.52	+57 12 20.0	0.188	0.270	15.30	9.26	− 3.9	10.65	2.12	− 5.3	0.0270	G	
LHW J104530+583828	10 45 30.85	+58 38 28.4	0.515	0.535	10.70	9.56	5.4	0.00	0.00	0.0	0.0251	G	

Notes.

The format is the following: Column (1): source IAU name. The components of multiple sources are labelled 'A', 'B', etc. Columns (2) and (3): source position: right ascension and declination (J2000). Column (4): source 1.4 GHz peak flux density, in mJy. Column (5): source 1.4 GHz integrated flux density, in mJy. Columns (6) and (7): fitted major and minor axes (FWHM) of the source in arcsec. Column (8): fitted position angle (PA, measured N through E) for the major axis in degrees. Columns (9) and (10): deconvolved major and minor axes (FWHM) of the source in arcsec. Zero values refer to unresolved (or partially unresolved) sources. Column (11): deconvolved position angle (PA, measured N through E) for the major axis in degrees. Zero values refer to unresolved sources. Column (12): source local noise (σ_{local}) in mJy. Column (13): fitting Flag. Flag indicating the fitting procedure and parametrization adopted for the source or source component. *G* refers to Gaussian fit. *E* refers to non-Gaussian sources. *M* refers to global parameters of multiple sources (see the text for more details). Column (14): morphology flag. An additional flag is given in some specific cases: (1) * when the Gaussian fit is poor (see Section 4 for more details); (2) *c* when the source is well fitted by a Gaussian but shows signs of a more *complex* morphology; (3) *m* when the source is catalogued as a single source, but shows signs of *multiple* components; and (4) *n* when a source appears to be spurious (*noise* artefact).

measurements for point sources ($\vartheta_{\rm maj} \times \vartheta_{\rm min} = 11$ arcsec $\times$ 9 arcsec, PA $= 0^\circ$):

$$\sigma(S_{\rm peak})/S_{\rm peak} = 1.00 \left(\frac{S_{\rm peak}}{\sigma}\right)^{-1} \quad (4)$$

$$\sigma(\theta_{\rm maj})/\theta_{\rm maj}) = 1.11 \left(\frac{S_{\rm peak}}{\sigma}\right)^{-1} \quad (5)$$

$$\sigma(\theta_{\rm min})/\theta_{\rm min}) = 1.11 \left(\frac{S_{\rm peak}}{\sigma}\right)^{-1} \quad (6)$$

As demonstrated in Prandoni et al. (2000b), the fact that a source is extended does not affect the internal accuracy of the fitting algorithm and therefore the errors quoted above apply to fitted flux densities and source sizes of extended sources as well.

Similar equations hold for position 1σ internal errors (Condon 1997; Condon et al. 1998), that applied to point sources in our radio survey, reduce to:

$$\sigma(\alpha) = 3.46 \left(\frac{S_{\rm peak}}{\sigma}\right)^{-1} \quad \text{(arcsec)} \quad (7)$$

$$\sigma(\delta) = 5.16 \left(\frac{S_{\rm peak}}{\sigma}\right)^{-1} \quad \text{(arcsec)} \quad (8)$$

Calibration terms are in general estimated from comparison with external data of better accuracy than the one tested. As discussed in Section 2, the LH region has been observed at 1.4 GHz by previous smaller surveys, using the VLA. In addition, the region is covered by shallower VLA all sky surveys like the NVSS (Condon et al. 1998) and the FIRST (Becker et al. 1995). None of such surveys can in principle be considered of better accuracy than our survey. Nevertheless, a source flux density/position comparison with those samples, allows us to check the consistency of our parameter measurements and calibration with those of the other existing surveys, and check for any systematic effects that we might have introduced in the image processing (especially at low signal-to-noise values).

5.1 Comparison with external data

Our source catalogue was cross-correlated with the shallow NVSS and FIRST all-sky catalogues (limiting fluxes ∼2.5 and ∼1 mJy respectively) and with three other deeper overlapping catalogues (as described in Section 2): de Ruiter et al. (1997, VLA C-configuration); Ibar et al. (2009, VLA mostly B-configuration); and Biggs & Ivison (2006, VLA A+B-configurations).

The results of this comparison are shown in Figs 8 and 9. In Fig. 8, we have plotted the WSRT against the other catalogue flux densities for all common sources. The plot shows that, despite the different intrinsic resolution of the various surveys (as indicated in the plot panels), the WSRT flux scale is in very good agreement with the NVSS, FIRST, de Ruiter et al. (1997) and Ibar et al. (2009) ones over the entire flux range probed by the different samples. This allows us to conclude that our flux calibration errors are within a few per cent, in line with expectations, and that no systematic effects have been introduced in the image deconvolution process. On the other hand, the comparison with Biggs & Ivison (2006) shows that our sample is characterized by systematically higher flux densities. This may be partly due to the significantly different resolution of the two catalogues (∼10 arcsec against 1.3 arcsec). A similar trend was found by Ibar et al. (2009) when comparing their catalogue with the Biggs & Ivison one. From a detailed analysis of the two samples, Ibar et al. however concluded that the systematic differences in flux measurements were to be ascribed to the different approaches used for the source extraction. In particular, Biggs & Ivison (2006) used a fixed beam size to fit a Gaussian to sources which were assigned areas smaller than the beam by the initial extraction procedure. This inevitably yields lower flux measurements (see Ibar et al. 2009 for more details).

A similar comparison was repeated for source positions and the result is plotted in Fig. 9. Again, the source positions derived for our source catalogue are in very good agreement with those derived for the comparison samples obtained at the VLA and with different calibration strategies. Systematic offsets, if present, can be considered negligible (±0.01–0.1 arcsec) with respect to the intrinsic position measurement errors of both our (see equations 7 and 8) and comparison catalogues. The only exception is represented by the de Ruiter et al. (1997) sample, where larger systematic offsets ($\Delta\alpha = -0.5$ arcsec and $\Delta\delta = -0.6$ arcsec) are found. However such systematic errors are more likely to be ascribed to the de Ruiter et al. catalogue, since no significant trend is found in the comparison with the other samples. In summary, we can conclude that our source position calibration strategy (through the use of a VLBA secondary calibrator) was successful, and that our reduction strategy has not introduced significant systematic offsets. This is of particular relevance for cross-identification purposes (with other radio and/or optical/IR catalogues), which is an obvious subsequent step for a full scientific exploitation of our sample.

6 SOURCE SIZES AND RESOLUTION BIAS

Fig. 10 shows the source Gaussian deconvolved angular sizes as a function of flux density for our sample. The solid line in Fig. 10 indicates the minimum angular size, $\Theta_{\rm min}$, below which sources are considered point-like, as derived from equations (1) and (2) (see Section 4.3 for more details). In general, we can successfully deconvolve ∼60 per cent of the sources in our sample, ∼80 per cent of the sources with $S \geq 0.7$ mJy and ∼90 per cent of the sources with $S \geq 2.5$ mJy. Above such flux limits, where we have a limited number of upper limits, we can reliably undertake a statistical analysis of the source size properties. To this extent, we compare the median angular size measured in different flux intervals for the sources with $S \geq 0.7$ mJy (black points) and the angular size integral distribution derived for the sources with $1 < S$ (mJy) < 100 (dotted–dashed line in the inner panel) to the ones obtained from the Windhorst, Mathis & Neuschaefer (1990) relations proposed for deep 1.4 GHz samples: $\Theta_{\rm med} = 2$ arcsec $\times$ $(S_{1.4\rm GHz})^{0.30}$ (S in mJy) and $h(>\Theta) = \exp[-\ln 2\,(\Theta/\Theta_{\rm med})^{0.62}]$. We notice that the Windhorst et al. relations are widely recognized to provide good statistical descriptions of source sizes at flux densities $\gtrsim 1$ mJy, i.e. at the flux levels probed by our analysis. Indeed our determinations show a very good agreement with the ones of Windhorst et al. (1990; see dashed lines in Fig. 10).

We notice that flux losses in extended sources can in principle affect our source parametrization and cause incompleteness in the source catalogue itself. In fact, a resolved source of given $S_{\rm tot}$ will drop below the peak flux density detection threshold more easily than a point source of same $S_{\rm tot}$. This is the so-called *resolution bias*. Equation (2) can be used to give an approximate estimate of the maximum size ($\Theta_{\rm max}$) a source of given $S_{\rm tot}$ can have before dropping below the $S_{\rm peak} = 5\sigma_{\rm local}$ limit of the source catalogue. Such a limit is represented by the black dotted–dashed line plotted in Fig. 10. As expected, the angular sizes of the largest sources approximately follow the estimated $\Theta_{\rm max}-S_{\rm tot}$ relation.

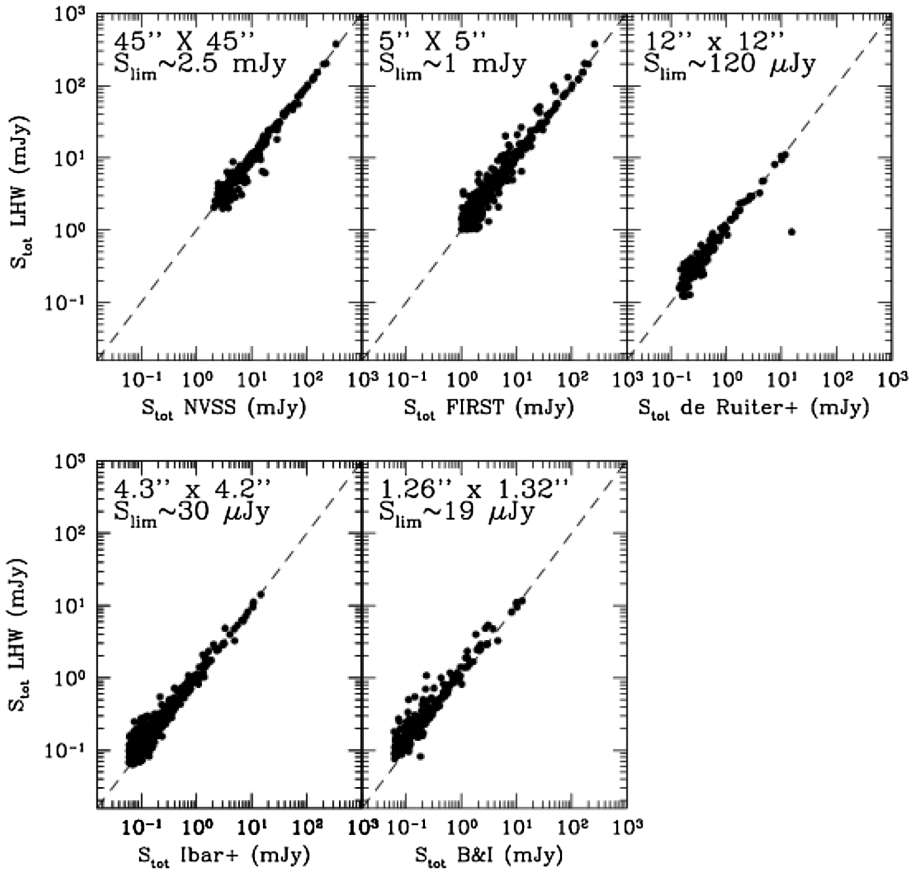

Figure 8. Flux comparison between our sample and other existing overlapping catalogues. The limiting flux and the spatial resolution of comparison samples are reported in each panel. See the text for more details.

In principle, there is a second incompleteness effect, related to the maximum scale at which our WSRT mosaics are sensitive due to the lack of baselines shorter than 36 m. This latter effect can, however, be neglected in our case, because it is smaller than the previous one over the entire flux range spanned by the survey. In fact, we expect the sample to become progressively insensitive to source scales larger than 500 arcsec. Moreover, if we assume the angular size distribution proposed by Windhorst et al. (1990) we expect no sources with $\Theta > 500$ arcsec in the area and flux range covered by our survey.

7 SOURCE COUNTS AT 1.4 GHz

We start by limiting the source count derivation to the mosaic region with local rms noise <330 μJy (see discussion in Section 4), corresponding to a total area of ∼6 deg^2. We used all sources brighter than 70 μJy (corresponding to $\gtrsim 6\sigma$ in the deepest part of the mosaic) to derive the differential source counts as a function of flux density. This minimizes flux boosting and incompleteness issues at the 5σ catalogue extraction threshold (see Section 4). Integrated flux densities were used for extended sources and peak flux densities for point-like sources. Each source has been weighted by the reciprocal of its visibility area ($A(> S_{\rm peak})/A_{\rm tot}$), as derived from Fig. 2 (right-hand panel), by setting $S_{\rm peak} > 5\sigma_{\rm local}$. This is the fraction of the total area over which the source could be detected.

Moreover, we have taken into account both the catalogue contamination introduced by artefacts (see discussion in Section 4.1), and the catalogue incompleteness, due to the resolution bias discussed in the previous section. The correction c for the resolution bias has been defined following Prandoni et al. (2001) as:

$$c = 1/[1 - h(>\Theta_{\rm lim})] \quad (9)$$

where $h(>\Theta_{\rm lim})$ is the integral angular size distribution proposed by Windhorst et al. (1990) for 1.4 GHz samples, which turned out to be a good representation of the source sizes at least down to $S \sim 0.7$ mJy (see Section 6). $\Theta_{\rm lim}$ represents the angular size upper limit, above which we expect to be incomplete. This is defined as a function of the integrated source flux density as (see Prandoni et al. 2001):

$$\Theta_{\rm lim} = \max[\Theta_{\rm min}, \Theta_{\rm max}] \quad (10)$$

where $\Theta_{\rm min}$ and $\Theta_{\rm max}$ are the parameters defined in Section 8. The $\Theta_{\rm min}-S$ relation (solid line in Fig. 10) is important at low flux levels where $\Theta_{\rm max}$ (black dotted–dashed line in Fig. 10) becomes unphysical (i.e. $\rightarrow 0$). In other words, introducing $\Theta_{\rm min}$ in the equation takes into account the effect of having a finite synthesized beam size (that is $\Theta_{\rm lim} \gg 0$ at the survey limit) and a deconvolution efficiency which varies with the source peak flux.

The differential source counts normalized to a non-evolving Euclidean model (n $S^{2.5}$) are listed in Table 2 and shown in Fig. 11 (filled black circles). Our source counts are compared with others available at 1.4 GHz from the literature, either in the LH region (de Ruiter et al. 1997; Biggs & Ivison 2006; Owen & Morrison 2008; Ibar et al. 2009) or in other regions of the sky. This includes all known deep fields, from single pointings like the 13 h

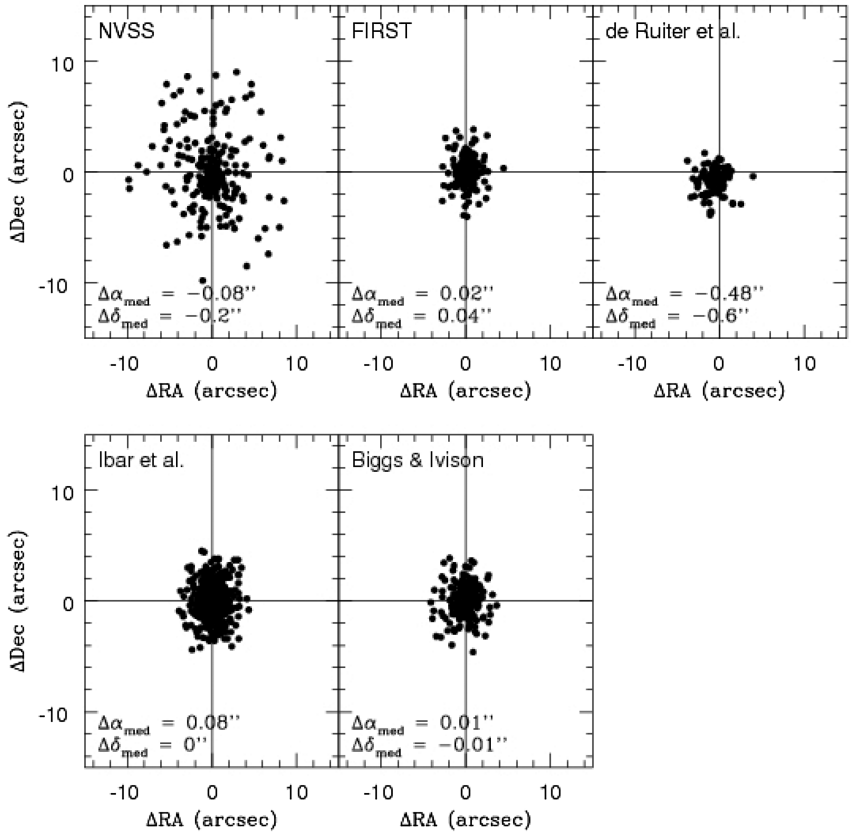

Figure 9. Comparison of source positions between our sample and other existing overlapping catalogues. Median values for ΔRA and ΔDec. are reported in each panel.

XMM field (Seymour, McHardy & Gunn 2004), the Hubble Deep Field (HDF) South and North (Huynh et al. 2005; Biggs & Ivison 2006), the European Large-Area ISO Survey North 2 (ELAIS N2; Biggs & Ivison 2006), the Subary XMM-BNewton Deep Field (SXDF; Simpson et al. 2006), the Small Selected Area 13 (SSA13; Fomalont et al. 2006), and the Extended Chandra Deep Field South (ECDFS; Padovani et al. 2015), to wider-area (>1 deg^2) regions, like the Phoenix Deep Field (PDF; Hopkins et al. 2003), the VLA VIMOS VLT Deep Survey (VLA-VVDS; Bondi et al. 2003), the VLA-COSMOS (Bondi et al. 2008), the At-Large Area Survey (ATLAS; Hales et al. 2014), to shallower large ($\gg$10 deg^2) surveys like the Australia Telescope ESO Slice Project (ATESP; Prandoni et al. 2001), the SDSS Stripe 82 (Heywood et al. 2016), and the FIRST survey (White et al. 1997). Also shown are the source counts derived from the semi-empirical sky simulation developed in the framework of the SKA Simulated Skies project (S3-SEX, Wilman et al. 2008, 2010; solid line), which represent the summed contribution of the modelling of various source populations (RL and RQ AGNs; SFGs).

Fig. 11 illustrates very well the long-standing issue of the large scatter (exceeding Poisson fluctuations) present at flux densities $\lesssim$ 1 mJy. The main causes for this considerable scatter can be either cosmic variance (source clustering) or survey systematics introduced by e.g. calibration, deconvolution, and source extraction algorithms, or corrections applied to raw data to derive the source counts. These issues have been extensively discussed in the recent literature. Heywood et al. (2013) compared the observed source counts with samples of matching areas extracted from the S3-SEX simulations (Wilman et al. 2008, 2010), that include a recipe for source clustering, and concluded that the observed scatter is dominated by cosmic variance, at least down to 100 μJy. This is clearly illustrated by the pink shaded area shown in Fig. 11, showing the predicted source counts' spread due to cosmic variance for typical areas of deep radio fields. This has been obtained by splitting the S3-SEX simulation in 400 0.5-deg^2 fields.

There are however a few exceptions. The most notable one is the anomalously high number counts estimate obtained by Owen & Morrison (2008) in the LH 1046+59 field (filled blue squares in Fig. 11). New confusion-limited, lower resolution VLA observations of the same field obtained at 3 GHz demonstrated that this is the result of an overestimated resolution bias correction (Condon et al. 2012; Vernstrom et al. 2014). Another exception could be the counts' estimate obtained in the LH region by Biggs & Ivison (2006, cyan squared crosses), which tends to be low (even if still consistent with cosmic variance). As we demonstrated in Section 5, this sample suffers from flux underestimations. Also in this case, the low counts are more likely to be ascribed to technical problems, rather than mere cosmic variance.

8 CONSTRAINTS FROM WIDE-AREA SOURCE COUNTS

A more robust view of the 1.4 GHz source counts can be obtained by using the widest area samples available to date. Cosmic variance depends on a combination of area coverage and depth. For a

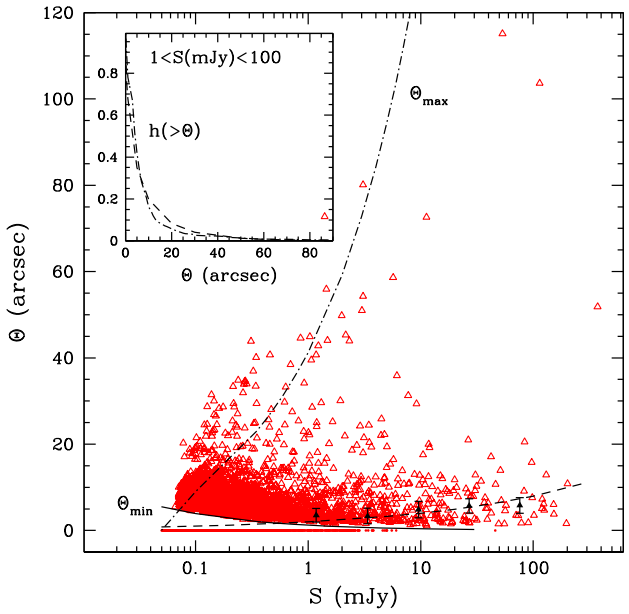

Figure 10. Deconvolved angular size (Θ=Θ_{maj}) as a function of integrated flux density (for unresolved sources we assume S_{tot}=S_{peak}). The dotted–dashed line represents the size (Θ_{max}), above which the sample becomes incomplete, due to the resolution bias. The solid line indicates the minimum angular size (Θ_{min}), below which deconvolution is not considered meaningful. The dashed line indicates the median source size as a function of flux as expected from Windhorst et al. (1990) relation. Such line has to be compared to the black points which represent the median source sizes for different flux intervals, as measured in our sample. The inner panel shows the angular size integral distribution ($h(>\Theta)$) proposed by Windhorst et al. (1990; dashed line), compared to the integral size distribution of sources in our sample (dotted–dashed line).

Table 2. 1.4 GHz source counts as derived from our survey. The format is the following: Column 1: flux interval (ΔS); Column 2: geometric mean of the flux density ($\langle S \rangle$); Column 3: number of sources detected (N_S); and Column 4: differential counts normalized to a non-evolving Euclidean model (n $S^{2.5}$). Also listed are the Poissonian errors (calculated following Regener 1951) associated with the normalized counts.

ΔS (mJy)	$\langle S \rangle$ (mJy)	N_S	dN/dS $S^{2.5} \pm \sigma$ (sr^{-1}Jy$^{1.5}$)
0.070–0.121	0.092	1896	$4.32^{+0.10}_{-0.10}$
0.121–0.210	0.160	1462	$5.17^{+0.14}_{-0.14}$
0.210–0.364	0.276	801	$5.12^{+0.18}_{-0.19}$
0.364–0.630	0.479	457	$5.69^{+0.27}_{-0.28}$
0.630–1.091	0.829	282	$7.30^{+0.43}_{-0.46}$
1.091–1.890	1.436	181	$10.14^{+0.75}_{-0.81}$
1.890–3.274	2.487	100	$11.7^{+1.2}_{-1.3}$
3.274–5.670	4.308	67	$18.5^{+2.3}_{-2.5}$
5.670–9.821	7.462	42	$26.6^{+4.1}_{-4.7}$
9.821–17.01	12.92	41	$59.4^{+9.3}_{-10.7}$
17.01–29.46	22.39	22	73^{+16}_{-19}
29.46–51.03	38.77	11	84^{+25}_{-33}
51.03–88.39	67.16	13	224^{+62}_{-79}
88.39–153.1	116.3	10	391^{+124}_{-163}
153.1–265.2	201.5	5	356^{+159}_{-230}

given allowed cosmic variance, the deeper the survey, the larger the volume sampled, the smaller the area coverage requirement. Fig. 12 shows the source counts derived from the largest 1.4 GHz surveys obtained so far and fully sensitive to the flux range ∼0.1–1 mJy (COSMOS, PDF, and this work), together with the largest surveys that probe flux densities $\gtrsim$ 1 mJy (ATESP, Stripe 82, and FIRST). Fig. 12 clearly shows that the scatter below 1 mJy is considerably reduced, when limiting to widest area surveys, and is mostly consistent with Poisson fluctuations. Our LH survey (counts derived over ∼6 deg^2) provides the most robust statistics between ∼0.1 and 1 mJy, while the FIRST (1550 deg^2) provides excellent estimates above a few mJy. Recent wide-area, deep surveys obtained at frequencies different from 1.4 GHz (like e.g. the VLA-COSMOS 3 GHz Large Project – Smolčić et al. 2017 – or the Australia Telescope Compact Array XMM Extragalactic (ATCA-XXL) Survey at 2.1 GHz – Butler et al. 2017) are not included here to avoid introducing unwanted uncertainties or systematic effects. The extrapolation of the counts to 1.4 GHz is very sensitive to the assumed spectral index. In addition adopting the same (average or median) spectral index value for all the sources may not be appropriate. There are indeed indications that the spectral index may flatten at mJy/sub-mJy regimes (e.g. Prandoni et al. 2006; Whittam et al. 2013) and re-steepen again at μJy levels, depending on the flux-dependent AGN/SFG source mix (e.g. Owen et al. 2009). The only exception we make is for the analysis performed at 3 GHz in the LH 1046+59 field by Vernstrom et al. (2014) that provides the most reliable constraint available so far down to flux densities $\lesssim$ 10 μJy. This counts determination is obtained from the so-called $P(D)$ analysis, which allows to investigate the source statistical properties well below the confusion limit of the survey. As such, the $P(D)$ analysis tends to be less prone to resolution effects, as well as to cosmic variance (as it probes larger volumes), and can provide more reliable results even in case of limited survey areas. The source counts derived from wide-area sub-mJy surveys are fully consistent with the results of the $P(D)$ analysis of Vernstrom et al. (2014).

The only remaining uncertainties are around the knee of the distribution (∼1 mJy), where the shallower surveys seem to suffer from incompleteness, and some discrepancy is found between the various surveys.

The measured source counts tend to be higher than the predicted model from Wilman et al. (2008, 2010, black solid line) in the flux range 10–400 μJy. This discrepancy appears statistically significant and cannot be accounted for by mere cosmic variance, whose effects on 5 and 10 deg^2 survey scales are illustrated by the light and dark blue shaded regions, respectively. The $P(D)$ analysis of Vernstrom et al. (2014) suggests that the observed excess may be present down to very faint flux densities.

In order to assess which component of the faint radio population is most likely responsible for the measured excess observed in the source counts below a few hundreds μJy, we exploited the multi-wavelength information available in the LH region. This allowed us to get a first characterization of the radio sources extracted from our mosaic. The identification and classification process will be fully discussed in a forthcoming paper, where the multiband properties of the faint radio population in the LH field will be presented. Here, we only summarize in broad terms the method followed and the diagnostics used.

In order to identify the counterparts of the WSRT 1.4 GHz sources we used the so-called *SERVS Data Fusion* (Vaccari et al. 2010; Vaccari 2015), a mid-IR-selected catalogue combining the far-UV-to-sub-millimetre data sets described in Section 2, as well as the available photometric and spectroscopic redshifts. Since we

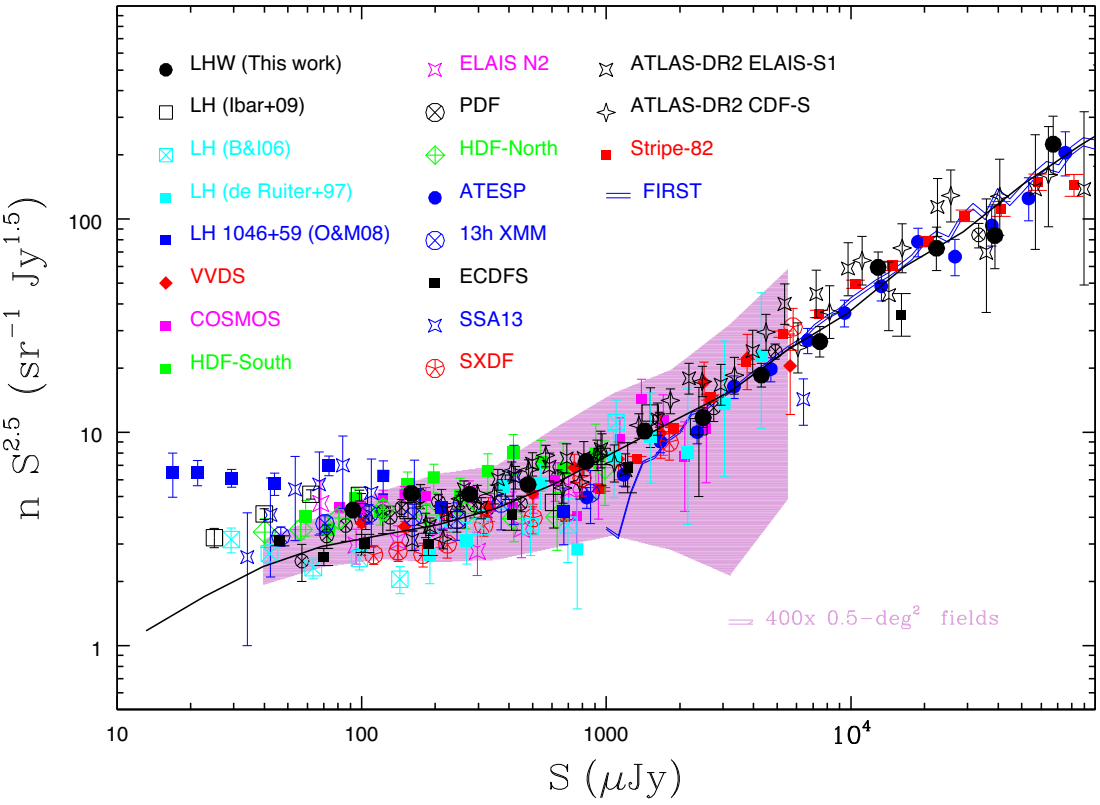

Figure 11. Normalized 1.4 GHz differential source counts for different samples (as indicated in the figure and in the text). The counts derived from the catalogue discussed in this work are represented as filled black circles. Vertical bars represent Poissonian errors on the normalized counts. Also shown are the source counts derived from 200 deg^2 of the semi-empirical simulation of Wilman et al. (2008, S3-SEX, solid line), which represent the summed contribution of the modelling of various source populations (RL and RQ AGNs; SFGs), and the predicted spread due to cosmic variance for 0.5 deg^2 fields (pink shaded area). They have been obtained by splitting the S3-SEX simulation in 400 0.5-deg^2 fields.

are interested to probe the counts' sub-mJy regime we limited our analysis to the inner ∼2 deg^2 of our mosaic, where a roughly uniform rms noise of ∼11 μJy is measured (see Section 3.1), and which is fully covered by the UKIDSS-DXS deep *K*-band mosaic (Lawrence et al. 2007). In addition only radio sources brighter than 120 μJy (i.e. with S/N $>10\sigma$) were considered. This was motivated by the relatively poor resolution of our WSRT observations (∼10 arcsec) which results in positional errors of the order of ∼1 arcsec at the faintest (5σ) limit of the radio catalogue (see Section 5). This, combined with the high number density of the confusion-limited SERVS data set, that prevents us to push our identification search beyond 1.5–2 arcsec (to keep contamination under control), means that our identification procedure gets progressively incomplete going to lower flux densities. At 120 μJy, we estimate the incompleteness to be $\sim 10-15$ per cent. In summary, we restricted our sample to 1110 single-component radio sources, 80 per cent of which were identified. For the reasons outlined above, we did not attempt a matching of the multicomponent radio sources, as the error associated to their position is even larger (typically of the order of few arcseconds). Nevertheless, we know that multicomponent sources are radio galaxies. We can therefore directly assign these latter sources (45 with $S > 120$ μJy) to the RL AGN class.

The identified single-component radio sources were classified using multiband diagnostics, as described below. We first identified the RL AGN component, and then proceeded with the separation of SFGs from AGNs in the remaining RQ population. RL AGNs were primarily identified through their radio excess. In particular we used the well-known method based on the observed 24 μm to 1.4 GHz flux density ratio ($q_{24\,\mathrm{obs}} = \log[S_{24\,\mu\mathrm{m}}/S_{1.4\,\mathrm{GHz}}]$; see Bonzini et al. 2013). For each source, the $q_{24\,\mathrm{obs}}$ parameter is compared to the one expected for SFGs as a function of redshift (as illustrated in Fig. A1). Sources not detected at 24 μm, and characterized by 24 μm to 1.4 GHz flux density ratio upper limits not stringent enough for a reliable classification, were classified based on their red IRAC colours (i.e. their 8.0–4.5 μm and 5.8–3.6 flux density ratios; see Luchsinger et al. 2015 for more details). In the recent literature RQ AGNs in deep radio-selected samples are separated from SFGs based on their IRAC colours and, when available, X-ray luminosities (see e.g. Bonzini et al. 2013). In the LH region, the X-ray band information is limited to the two deep fields observed by *XMM* and *Chandra* (see Fig. 1), and both are located at the periphery of our 1.4 GHz mosaic. We therefore decided to complement the IRAC-colour-based classification (Lacy et al. 2004, 2007; Stern et al. 2005; Donley et al. 2012; see example in Fig. A2) with other diagnostic diagrams discussed in the literature, that combine IRAC with *Herschel* or *K*-band information (e.g. Kirkpatrick et al. 2012; Messias et al. 2012). The latter (shown in Fig. A3) proved to be particularly useful, thanks to the high detection rate at *K* band of our identified sources (∼90 per cent). The above procedures allowed us to classify 99 per cent of the identified sources.

The results in terms of source counts are illustrated in Fig. 13, where we compare the counts obtained from the identified sources in our sample (split in several sub-components) to those expected from the S3-SEX simulations, after applying the same cut in magnitude

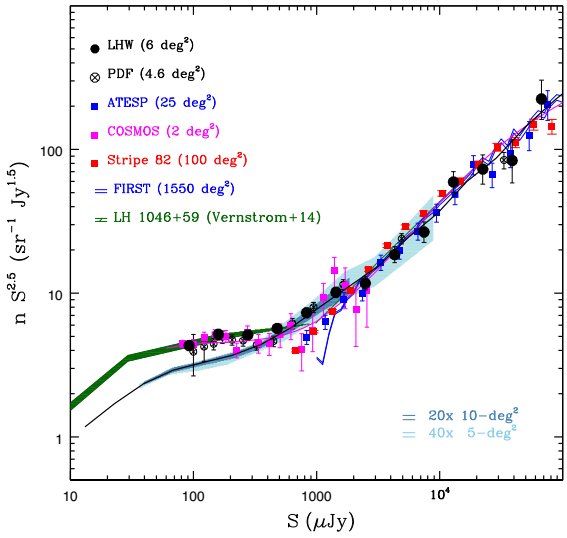

Figure 12. Normalized 1.4 GHz differential source counts from large-scale surveys (as indicated in the figure). Vertical bars represent Poissonian errors on the normalized counts. Also shown is the result of the $P(D)$ analysis performed by Vernstrom et al. (2014, dark green shaded area). In this case, the counts are rescaled from 3 to 1.4 GHz by assuming $\alpha = -0.7$. The black solid line represents the predicted counts from 200 deg^2 of the S3-SEX simulations (Wilman et al. 2008), while the magenta solid line represents the fit obtained by Bondi et al. (2008) from the COSMOS and FIRST source counts. The light and dark blue shaded areas illustrate the predicted cosmic variance effects for survey coverages of 5 and 10 deg^2, respectively. They have been obtained by splitting the S3-SEX simulation in forty 5-deg^2 and twenty 10-deg^2 fields, respectively.

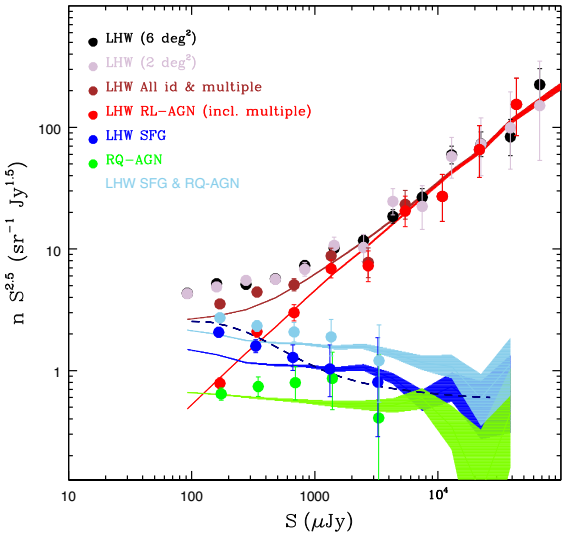

Figure 13. Normalized 1.4 GHz differential source counts obtained in the inner $\sim$2 deg^2 region of our mosaic split in sub-components (filled points) compared to the S3-SEX predictions for a 200 deg^2 region (solid lines/bands): All radio sources (grey); identified radio sources, including unidentified multicomponent sources (brown); RL AGNs, including unidentified multicomponent sources (red); SFGs (blue); RQ AGNs (green); and RQ population as a whole (obtained by summing SFGs and RQ AGNs, light blue). For a meaningful comparison, we applied the same magnitude cut ($11 < K_{\rm Vega} < 21.5$) to both our identified radio sources and the S3-SEX catalogues. For the SFG population, an additional comparison model is shown (dark-blue dashed line; Mancuso et al. 2017). The counts obtained in the inner $\sim$2 deg^2 region (grey filled points) are fully consistent with those obtained from the full mosaic (6 deg^2, black filled points). Vertical bars represent Poissonian errors on the normalized counts.

to both our identified sample and the S3-SEX simulations ($11 < K_{\rm Vega} < 21.5$). RL AGNs (red points) nicely follow the S3-SEX predictions (red solid line) over the entire flux range probed by our sample. The RQ population (i.e. the sum of SFGs and RQ AGNs), on the other hand, show an excess with respect to the predicted counts below $\sim$500 μJy (see light blue points and solid line). The observed excess is marginal, but affected by the aforementioned incompleteness. When splitting the RQ population in its two main components, SFGs (shown in blue) and RQ AGNs (shown in green), the excess becomes more relevant for SFGs. RQ AGNs do show some excess at intermediate fluxes, but given the large error bars, it cannot be considered statistically significant. We caveat, though, that the selection criteria used to identify RQ AGN (essentially based on IR and K-band information) will miss objects that present AGN signatures only in the X-ray band or in their optical spectra. Therefore, we cannot exclude that some of the excess over the S3-SEX models, now entirely attributed to SFGs, might be associated with RQ-AGNs.

The SFG component in the S3-SEX simulations has been modelled starting from the well-constrained 1.4 GHz local luminosity function of SFGs (see e.g. Yun, Reddy & Condon 2001) and assuming a pure luminosity evolution of the form $(1+z)^{3.1}$ (for both normal and starburst galaxies) out to $z = 1.5$, with no further evolution thereafter. This evolutionary form can reproduce the observed number density in the local ($z < 0.3$) Universe (see e.g. Mauch & Sadler 2007), that dominate at flux densities $\gtrsim$ 2 mJy, and is consistent with other constraints obtained by combining the observed global SFR density evolution and the 1.4 GHz radio source counts (Hopkins 2004). Nevertheless our measured source counts suggest a somewhat steeper evolution for SFGs going to lower flux densities (or higher redshifts).

A full discussion of the evolutionary properties of radio-selected SFGs is beyond the scopes of this paper, but it is worth mentioning that a steeper evolution of SFGs is supported by the work of Mancuso et al. (2016, 2017), who proposed a novel model-independent approach, where they combine UV and far-IR data to trace the evolution of the intrinsic SFR function over the entire redshift range $z \sim 0-10$ (see Mancuso et al. 2016 for details). Their results are claimed to be less prone to dust extinction effects especially at high redshifts ($z > 3$) and at large SFRs ($\gtrsim 100$ M$_\odot$ yr^{-1}), where they predict a heavily dust-obscured galaxy population, in excess to what found by previous works. By using standard prescriptions to convert SFRs into 1.4 GHz luminosities, Mancuso et al. (2017) were able to get a novel prediction of the contribution of SFGs to 1.4 GHz source counts. Interestingly, Mancuso et al. (2017) prediction (dark blue dashed line) seems to better reproduce the shape of the observed SFG counts, providing a good match to both the excess at low flux densities (especially when considering the 10−20 per cent incompleteness of the sample), and the observations at brighter fluxes (progressively dominated by local radio sources).

For completeness, it is worth mentioning that other recent works (mainly based on the VLA-COSMOS 3 GHz Large Project; Smolčić et al. 2017) have proposed different models for radio-selected SFGs. For instance, Novak et al. (2017) found that their data are consistent with a pure luminosity evolution of the form $(1+z)^{3.16\pm0.2}$ out to the redshift limit of the survey (i.e. $z \sim 4-5$). In addition, they

report a negative evolution of the IR/radio correlation for SFGs. This evolution takes the form of $\sim(1+z)^{\alpha}$, with $\alpha = -0.14 \pm 0.01$. Bonato et al. (2017) claim that any evolution of the IR/radio correlation should be mild ($|\alpha| \lesssim 0.16$), as larger values would produce total source counts, inconsistent with the ones observed.

9 SUMMARY AND FUTURE PERSPECTIVES

In this paper, part of the LH Project, we have presented a deep 1.4 GHz mosaic of the LH area obtained using the WSRT. The final image covers an area of 6.6 deg^2, has a resolution of 11 x 9 arcsec and reaches an rms of 11 μJy beam^{-1} at the centre of the field. This is the widest area survey reaching such sensitivity so far. The catalogue extracted includes 6000 sources and it has already been exploited in a number of studies. For instance, Mahony et al. (2016) used it in combination with LOFAR 150 MHz data and other public catalogues for a multifrequency radio spectral analysis of the mJy radio population in the LH region. Brienza et al. (2017) expanded the radio spectral study to remnant radio AGNs in the same region.

The obtained source counts provide very robust statistics in the flux range $0.1 < S < 1$ mJy, and are in excellent agreement with other robust determinations obtained at lower and higher flux densities. Indeed, when considering only wide-area surveys the source counts are very well constrained down to $\gtrsim 10$ μJy. This allows us to start using source counts to constrain source evolutionary models; something that was prevented so far, due to the long-standing issue of the large scatter present at flux densities $\leq$1 mJy, and mainly motivated by cosmic variance (Heywood et al. 2013). Notably, the overall wide-area source counts show a clear excess with respect to the counts predicted by the semi-empirical radio sky simulations developed in the framework of the S3-SEX (Wilman et al. 2008, 2010), in the flux range 10–400 μJy. This discrepancy appears statistically significant and cannot be accounted for by cosmic variance.

Making use of the multiwavelength information available for the LH area, we have separated the sources in RL-AGN, RQ-AGN, and SFG and derived the source counts for these three separate groups. A preliminary analysis of the identified (and classified) sources suggests this excess is to be ascribed to SFGs, which seem to show a steeper evolution than predicted. The counts for RL and RQ AGN, on the other hand, appears to be in line with established models, like those implemented in the S3-SEX simulations. A steeper evolution of SFGs is supported by other recent observational work (e.g. Novak et al. 2017), and in particular by the novel model-independent approach proposed by Mancuso et al. (2016, 2017), who combine UV and far-IR data to trace the evolution of the intrinsic SFR function over the redshift range $z \sim 0-10$. A detailed and more complete analysis of the evolutionary properties of the LH sources, in comparison with other observational and modelling works will be the subject of a forthcoming paper. In the future, we also plan to make use of upgraded multiband information from the Herschel Extragalactic Legacy Project (Vaccari 2016).

The unique combination of sensitivity and area coverage of the WSRT LH mosaic, makes it ideal to be used as a test case for the exploitation of future wider area surveys obtained by new (or upgraded) radio facilities. Indeed, significantly larger but equally deep images will be obtained using the phased-array-feed system Apertif installed now on the WSRT array (Oosterloo et al. 2009) as well as ASKAP. It is worth to notice that the large field of view of Apertif will ensure a good match in spatial covering with LOFAR 150 MHz fields. The sensitivity of the two radio telescopes is also comparable for radio sources with typical spectral index of -0.7 (see Shimwell et al. 2017), opening exciting perspectives for statistical multifrequency studies of the faint radio sky.

Last but not least, new GHz telescopes like Apertif, ASKAP, and MeerKat offer broad-band capability that will allow to obtain simultaneously radio continuum and atomic neutral hydrogen, HI-21cm, information for the sources in the redshift range sampled by the observing band. Serendipitous H I detections in famous fields (e.g. the First Look Survey), have been already reported using data from traditional radio telescope like the WSRT (see Morganti et al. 2004) demonstrating the feasibility. A first stacking experiment to study the H I in various classes of radio sources in the LH area has also been presented in Geréb et al. (2013). The new generation of radio telescopes will make this a standard procedure expanding the information available for each class of galaxies.

ACKNOWLEDGEMENTS

IP thanks Claudia Mancuso for providing the evolutionary track shown in Fig. 13, which refers to the model discussed in Mancuso et al. (2017). This work has been supported by financial contribution from PRIN-INAF (2008) and from ASTRON. IP and MV acknowledge support from the Ministry of Foreign Affairs and International Cooperation, Directorate General for the Country Promotion (Bilateral Grant Agreements ZA14GR02 and ZA18GR02). RM gratefully acknowledges support from the European Research Council under the European Union's Seventh Framework Programme (FP/2007-2013)/ERC Advanced Grant RADIOLIFE-320745. This work is based on research supported by the National Research Foundation of South Africa (Grant Number 113121). The WSRT is operated by the Netherlands Institute for Radio Astronomy ASTRON, with support of NWO.

REFERENCES

Abolfathi B. et al., 2018, ApJS, 235, 42A
Baldwin J. A., Phillips M. M., Terlevich R., 1981, PASP, 93, 5
Becker R. H., White R. L., Helfand D. J., 1995, ApJ, 450, 559
Beichman C. A., Cutri R., Jarrett T., Steining R., Skrutskie M., 2003, AJ, 125, 2521
Bertin E., Arnouts S., 1996, A&AS, 117, 393
Biggs A. D., Ivison R. J., 2006, MNRAS, 371, 963
Blundell K. M., Kuncic Z., 2007, ApJ, 668, L103
Bonato M. et al., 2017, MNRAS, 469, 1912
Bondi M., Ciliegi P., Schinnerer E., Smolčić V., Jahnke K., Carilli C., Zamorani G., 2008, ApJ, 681, 1129
Bondi M. et al., 2003, A&A, 403, 857
Bonzini M., Padovani P., Mainieri V., Kellermann K. I., Miller N., Rosati P., Tozzi P., Vattakunnel S., 2013, MNRAS, 436, 3759
Bonzini M. et al., 2015, MNRAS, 453, 1079
Booth R. S., Jonas J. L., 2012, Afr. Skies, 16, 101
Brienza M. et al., 2017, A&A, 606, 98
Brunner H., Cappelluti N., Hasinger G., Barcons X., Fabian A. C., Mainieri V., Szokoly G., 2008, A&A, 479, 283
Butler A. et al., 2017, A&A, (in press)
Chambers K. C., Miley G. K., Van Breugel W. J. M., Bremer M. A. R., Huang J.-S., Trentham N. A., 1996, ApJS, 106, 247
Ciliegi P., Zamorani G., Hasinger G., Lehmann I., Szokoly G., Wilson G., 2003, A&A, 398, 901
Condon J. J., 1992, ARA&A, 30, 575
Condon J. J., 1997, PASP, 109, 166
Condon J. J., Cotton W. D., Greisen E. W., Yin Q. F., Perley R. A., Taylor G. B., Broderick J. J., 1998, AJ, 115, 1693
Condon J. J., Kellermann K. I., Kimball A. E., Ivezić ., Perley R. A., 2013, ApJ, 768, 37

Condon J. J. et al., 2012, ApJ, 758, 23
Coppin K. et al., 2006, MNRAS, 372, 1621
Delvecchio I. et al., 2017, A&A, 602, A3
de Ruiter H. R. et al., 1997, A&A, 319, 7
Donley J. L. et al., 2012, ApJ, 748, 142
Duncan K. J., Jarvis M. J., Brown M. J. I., Röttgering H. J. A., 2018b, MNRAS, 477, 5177
Duncan K. J. et al., 2018a, MNRAS, 473, 2655
Fazio G. et al., 2004, ApJS, 154, 10
Fomalont E. B., Kellermann K. I., Cowie L. L., Capak P., Barger A. J., Partridge R. B., Windhorst R. A., Richards E. A., 2006, ApJS, 167, 103
Garn T. S., Green D. A., Riley J. M., Alexander P., 2008a, MNRAS, 383, 75
Garn T. S., Green D. A., Riley J. M., Alexander P., 2008b, MNRAS, 387, 1037
Garn T. S., Green D. A., Riley J. M., Alexander P., 2010, Bull. Astron. Soc. India, 38, 103
Geréb K., Morganti R., Oosterloo T. A., Guglielmino G., Prandoni I., 2013, A&A, 558, A54
González-Solares E. A. et al., 2011, MNRAS, 416, 927
Gopal-Krishna, Patnaik A. R., Steppe H., 1983, A&A, 123, 107
Hales C. A. et al., 2014, MNRAS, 441, 2555
Hasinger G., Burg R., Giacconi R., Schmidt M., Trumper J., Zamorani G., 1998, A&A, 329, 482
Hasinger G. et al., 2001, A&A, 365, L45
Heckman T. M., Best P. N., 2014, ARA&A, 52, 589
Herrera Ruiz N., et al., 2017, A&A, 607, 132
Herrera Ruiz N., Middelberg E., Norris R. P., Maini A., 2016, A&A, 589, L2
Heywood I., et al., 2016, MNRAS, 460, 4433
Heywood I., Jarvis M. J., Condon J. J., 2013, MNRAS, 432, 2625
Holland W. S. et al., 1999, MNRAS, 303, 659
Hopkins A. M., 2004, ApJ, 615, 209
Hopkins A. M., Afonso J., Chan B., Cram L. E., Georgakakis A., Mobasher B., 2003, AJ, 125, 465
Huynh M. T., Jackson C. A., Norris R. P., Prandoni I., 2005, AJ, 130, 1373
Ibar E., Ivison R. J., Biggs A. D., Lal D. V., Best P. N., Green D. A., 2009, MNRAS, 397, 281
Jarvis, M. J. et al., 2001, MNRAS, 326, 1563
Johnston, S. et al., 2007, PASA, 24, 174
Kimball A. E., Kellermann K. I., Condon J. J., Ivezić ., Perley R. A., 2011, ApJ, 739, L29
Kirkpatrick A. et al., 2012, ApJ, 759, 139
Lacy M., Petric A. O., Sajina A., Canalizo G., Storrie-Lombardi L. J., Armus L., Fadda D., Marleau F. R., 2007, AJ, 133, 186
Lacy M. et al., 2004, ApJS, 154, 166
Lawrence A., Warren S. J., Almaini O., Edge A. C., Hambly N. C., Jameson R. F., Lucas P., Folger M., 2007, MNRAS, 379, 1599
Lockman F. J., Jahoda K., McCammon D., 1986, ApJ, 302, 432
Lonsdale C. J., Smith H. E., Rowan-Robinson M., Surace J., Shupe D., Xu C., Oliver S., Serjeant S., 2003, PASP, 115, 897
Luchsinger K. M. et al., 2015, AJ, 150, 87
Magliocchetti M., Maddox S. J., Lahav O., Wall J. V., 1998, MNRAS, 300, 257
Mahony E. K. et al., 2016, MNRAS, 463, 2997
Maini A., Prandoni I., Norris R. P., Giovannini G., Spitler L. R., 2016, A&A, 589, L3
Mainieri V., Bergeron J., Hasinger G., Lehmann H., Rosati P., Schmidt M., Szokoly G., Della Ceca R., 2002, A&A, 393, 425
Mancuso C., Lapi A., Shi J., Gonzalez-Nuevo J., Aversa R., Danese L., 2016, ApJ, 823, 128
Mancuso C. et al., 2017, ApJ, 842, 95
Martin D. C. et al., 2005, ApJ, 619, L1
Mauch T., Sadler E. M., 2007, MNRAS, 375, 931
Mauduit J.-C. et al., 2012, PASP, 124, 714
Messias H., Afonso J., Salvato M., Mobasher B., Hopkins A. M., 2012, ApJ, 754, 120
Mignano A., Prandoni I., Gregorini L., Parma P., Wieringa M. H., de Ruiter H. R., Vettolani G., Ekers R. D., 2008, A&A, 477, 449
Morganti R., Garrett M. A., Chapman S., Baan W., Helou G., Soifer T., 2004, A&A, 424, 371
Novak M. et al., 2017, A&A, 602, 5
Ocran E. F., Taylor A. R., Vaccari M., Green D. A., 2017, MNRAS, 468, 1156
Oliver S. J. et al., 2012, MNRAS, 424, 1614
Oosterloo T., Verheijen M. A. W., van Cappellen W., Bakker L., Heald G., Ivashina M., 2009, in Torchinsky S. A. et al., eds, Wide Field Astronomy Technology for the Square Kilometre Array, PoS(SKADS 2009)070
Owen F. N., Morrison G. E., 2008, AJ, 136, 1889
Owen F. N., Morrison G. E., Klimek M. D., Greisen E. W., 2009, AJ, 137, 4846
O'Dea C. P., 1998, PASP, 110, 493
Padovani P., 2016, A&ARv, 24, 13
Padovani P., 2017, NatAs, 1, 0194
Padovani P., Bonzini M., Kellermann K. I., Miller N., Mainieri V., Tozzi P., 2015, MNRAS, 452, 1263
Padovani P., Miller N., Kellerman K. I., Mainieri V., Rosati P., Tozzi P., 2011, ApJ, 740, 20
Padovani P. et al., 2009, ApJ, 694, 235
Polletta M., et al., , 2007, ApJ, 663, 81
Polletta M. et al., 2006, in Wilson A., ed., ESA SP-604: The X-ray Universe 2005. ESA Publications Division, Noordwijk, p. 807
Prandoni I., Gregorini L., Parma P., de Ruiter H. R., Vettolani G., Wieringa M. H., Ekers R. D., 2000a, A&AS, 146, 31
Prandoni I., Gregorini L., Parma P., de Ruiter H. R., Vettolani G., Wieringa M. H., Ekers R. D., 2000b, A&AS, 146, 41
Prandoni I., Gregorini L., Parma P., de Ruiter H. R., Vettolani G., Wieringa M. H., Ekers R. D., 2001, A&A, 365, 392
Prandoni I., Parma P., Wieringa M. H., de Ruiter H. R., Gregorini L., Mignano A., Vettolani G., Ekers R. D., 2006, A&A, 457, 517
Regener V. H., 1951, Phys. Rev. Lett., 84, 161L
Rieke G. et al., 2004, ApJS, 154, 25
Rottgering H. J. A., Lacy M., Miley G. K., Chambers K. C., Saunders R., 1994, A&AS, 108, 79
Rowan-Robinson M., Gonzalez-Solares E., Vaccari M., Marchetti L., 2013, MNRAS, 428, 1958
Rowan-Robinson M. et al., 2008, MNRAS, 386, 679
Sault R. J., Teuben P. J., Wright M. C. H ., 1995, in Shaw R. et al., eds, Astronomical Data Analysis Software and Systems IV, ASP Conf. Series, 77, p. 433
Seymour N., McHardy I. M., Gunn K. F., 2004, MNRAS, 352, 131
Seymour N. et al., 2008, MNRAS, 386, 1695
Shimwell T. W. et al., 2017, A&A, 598, A104
Simpson C. et al., 2006, MNRAS, 372, 741
Smolčić V. et al., 2008, ApJS, 177, 14
Smolčić V. et al., 2017, A&A, 602, 1
Snellen I. A. G., Schilizzi R. T., Miley G. K., de Bruyn A. G., Bremer M. N., Röttgering H. J. A., 2000, MNRAS, 319, 445
Stern D. et al., 2005, ApJ, 631, 163
Vaccari M., 2015, PoS, 267, 27
Vaccari M., 2016, The Universe of Digital Sky Surveys, Astrophysics and Space Science Proc., Vol. 42. Springer International Publishing, Switzerland, p. 71
Vaccari M. et al., 2010, A&A, 518, L20
Veilleux S, Osterbrock D. E., 1987, ApJS, 63, 295
Vernstrom T., Scott D., Wall J. V., Condon J. J., Cotton W. D., Kellermann K., Perley R., 2016b, MNRAS, 462, 2934
Vernstrom T., Scott D., Wall J. V., Condon J. J., Cotton W. D., Perley R., 2016a, MNRAS, 461, 2879
Vernstrom T. et al., 2014, MNRAS, 440, 2791
Werner M. et al., 2004, ApJS, 154, 1
White R. L., Becker R. H., Helfand D. J., Gregg M. D., 1997, ApJ, 475, 479
White S. V., Jarvis M. J., Häußler B., Maddox N., 2015, MNRAS, 448, 2665
White S. V., Jarvis M. J., Kalfountzou E., Hardcastle M. J., Verma A., Cao Orjales J. M., Stevens J., 2017, MNRAS, 468, 217

Whittam I. H. et al., 2013, MNRAS, 429, 2080
Wilman R. J., Jarvis M. J., Mauch T., Rawlings S., Hickey S., 2010, MNRAS, 405, 447
Wilman R. J. et al., 2008, MNRAS, 388, 1335
Windhorst R., Mathis D., Neuschaefer L., 1990, in Kron R. G., ed., ASP Conf. Ser., Vol. 10, Evolution of the Universe of Galaxies. Astron. Soc. Pac., San Francisco, p. 389
Yun M. S., Reddy N. A., Condon J. J., 2001, ApJ, 554, 803

SUPPORTING INFORMATION

Supplementary data are available at *MNRAS* online.

Table 1. The radio catalogue.

Please note: Oxford University Press is not responsible for the content or functionality of any supporting materials supplied by the authors. Any queries (other than missing material) should be directed to the corresponding author for the article.

APPENDIX: SOURCE CLASSIFICATION

In this appendix, we show the multiband diagnostic diagrams discussed in Section 8, where the source classification procedure is presented. The colour-coding in the figures refers to the final classification of the sources, based on the information at all available wavebands.

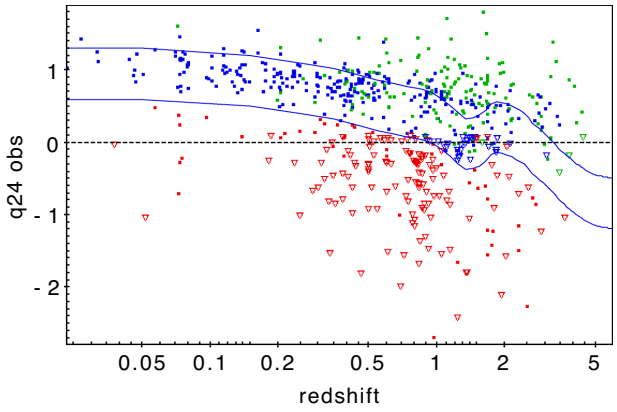

Figure A1. $q_{24\,\mathrm{obs}}$ values for the identified sources with $S \geq 0.12$ mJy with reliable redshift. For sources not detected at 24 μm, we set upper limits (downward triangles). The solid lines represent the redshifted M82 template normalized to the local average $q_{24\,\mathrm{obs}}$ value for SFGs (upper line), and the threshold adopted to identify RL AGN (lower line), defined by assuming a $\geq 2\sigma$ radio excess with respect to the M82 template. The sources which satisfy the radio loudness criterion are shown in red. The red upper limits above the adopted threshold are sources that have IRAC colours of elliptical galaxies (the typical hosts of radio galaxies) and that we added to the RL AGN class (see text for more details). The RQ population is divided in SFG (blue) and RQ AGN (green) as resulting from the classification procedure discussed in the text. The horizontal dotted line indicate the $q_{24\,\mathrm{obs}} \sim 0.0$ threshold assumed for sources with no redshift available (not plotted).

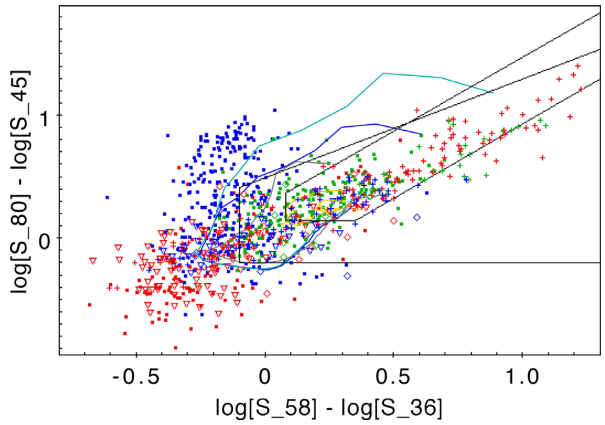

Figure A2. IRAC colour–colour diagram for the identified sources with $S \geq 0.12$ mJy: $\log S_{80} - \log S_{45}$ versus $\log S_{58} - \log S_{36}$. Source colour-coding is as follows: RQ-AGN (green); SFG (blue); and RL AGN (red). Sources detected at all four IRAC bands (3.6, 4.5, 5.8, and 8.0 μm) are shown as filled points; sources not detected at 8.0 μm only are shown as downward triangles; sources not detected at 5.8 μm only are shown as open diamonds; sources not detected at both 5.8 and 8.0 μm are shown as crosses. Sources detected only at one of the SERVS channels (3.6 or 4.5 μm) cannot be constrained and are not shown. The black solid lines represent the AGN wedges as defined by Lacy et al. (2004, 2007, larger wedge) and Donley et al. (2012, smaller wedge). Also shown are the redshifted SEDs for a number of prototypical classes (from Polletta et al. 2007). Line colour-coding is as follows: old (13 Gyr) elliptical galaxy (red); two SFG templates: M82 (blue) and Arp 220 (light blue); QSO (green); Seyfert 1 (orange) and Seyfert 2 (gray) galaxies. Redshift increases along the lines anticlockwise.

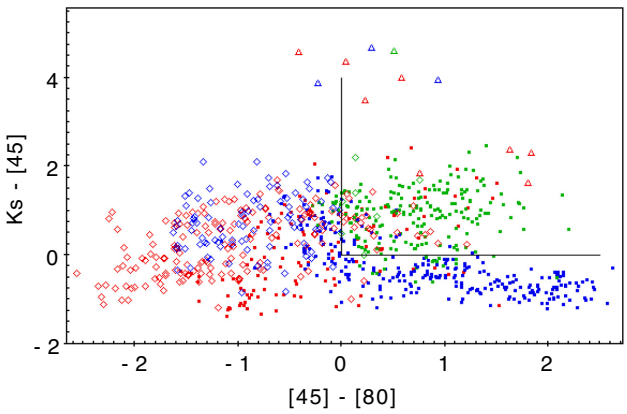

Figure A3. KI diagnostic plot for the identified sources with $S \geq 0.12$ mJy: 4.5–8.0 μm against $K_s - 4.5$ μm (all quantities are AB magnitudes). Source colour-coding as in Fig. A2. Sources detected at all three bands (K band, 4.5 and 8.0 μm) are shown as filled points; sources not detected at 8.0 μm only are shown as open diamonds; sources not detected at K band only are shown as upward triangles. Sources detected only at 4.5 μm are shown as crosses. Sources not detected at any of the three bands cannot be constrained and are not shown. The black solid lines represent the AGN wedge as defined by Messias et al. (2012).

This paper has been typeset from a TEX/LATEX file prepared by the author.